AGU PUBLICATIONS

JGR

Journal of Geophysical Research: Oceans

RESEARCH ARTICLE

10.1002/2014JC009837

Special Section:

Early scientific results from the salinity measuring satellites Aquarius/SAC-D and SMOS

Key Points:

- Geophysical model functions for L-band surface emission and radar backscatter
- Wind speed measurements with L-band sensors
- Surface roughness correction for ocean salinity retrievals

Supporting Information:

- Readme
- ts01
- ts02
- ts03
- ts04
- ts05

Correspondence to:

T. Meissner,
meissner@remss.com

Citation:

Meissner, T., F. J. Wentz, and L. Ricciardulli (2014), The emission and scattering of L-band microwave radiation from rough ocean surfaces and wind speed measurements from the Aquarius sensor, *J. Geophys. Res. Oceans*, *119*, 6499–6522, doi:10.1002/2014JC009837.

Received 22 JAN 2014
Accepted 19 AUG 2014
Accepted article online 23 AUG 2014
Published online 25 SEP 2014

The emission and scattering of L-band microwave radiation from rough ocean surfaces and wind speed measurements from the Aquarius sensor

Thomas Meissner[1], Frank J. Wentz[1], and Lucrezia Ricciardulli[1]

[1]Remote Sensing Systems, Santa Rosa, California, USA

Abstract In order to achieve the required accuracy in sea surface salinity (SSS) measurements from L-band radiometers such as the Aquarius/SAC-D or SMOS (Soil Moisture and Ocean Salinity) mission, it is crucial to accurately correct the radiation that is emitted from the ocean surface for roughness effects. We derive a geophysical model function (GMF) for the emission and backscatter of L-band microwave radiation from rough ocean surfaces. The analysis is based on radiometer brightness temperature and scatterometer backscatter observations both taken on board Aquarius. The data are temporally and spatially collocated with wind speeds from WindSat and F17 SSMIS (Special Sensor Microwave Imager Sounder) and wind directions from NCEP (National Center for Environmental Prediction) GDAS (Global Data Assimilation System). This GMF is the basis for retrieval of ocean surface wind speed combining L-band H-pol radiometer and HH-pol scatterometer observations. The accuracy of theses combined passive/active L-band wind speeds matches those of many other satellite microwave sensors. The L-band GMF together with the combined passive/active L-band wind speeds is utilized in the Aquarius SSS retrieval algorithm for the surface roughness correction. We demonstrate that using these L-band wind speeds instead of NCEP wind speeds leads to a significant improvement in the SSS accuracy. Further improvements in the roughness correction algorithm can be obtained by adding VV-pol scatterometer measurements and wave height (WH) data into the GMF.

1. Introduction

The goal of the Aquarius mission is to provide the science community with monthly SSS maps at 150 km spatial scale to an accuracy of 0.2 psu [*Lagerloef et al.*, 2008]. The basis of the Aquarius SSS retrieval algorithm [*Wentz et al.*, 2012] is to match the observed surface emissivity of a flat ocean surface with the Fresnel emissivity, which is calculated from a model of the permittivity of seawater [*Meissner and Wentz*, 2004, 2012]. The seawater permittivity itself depends on SSS, and this dependence is such that on a global scale the uncertainty in the surface brightness temperature (in Kelvin) translates into an SSS uncertainty (in psu) roughly as 1:2. That means that the 0.2 psu SSS accuracy requirement corresponds to a radiometric accuracy of about 0.1 K, which poses a very challenging task for the SSS retrieval algorithm.

One of the major drivers in the error budget of the SSS retrieval is the change of the ocean surface emission due to surface roughness. This roughness signal has to be removed from the Aquarius observation in order to obtain the emissivity of a specular ocean surface. The roughening is mainly caused by surface winds that result in large gravity waves, small capillary waves, and, at higher wind speeds, foam coverage of the ocean surface.

The functional dependence of emissivity on wind speed is called geophysical model function (GMF). Numerous empirical studies using various instruments and observation techniques have been performed to derive the GMF of this wind-induced surface emissivity signal, which is also known as excess emissivity. The first measurement of the L-band emissivity as function of wind speed was performed by *Hollinger* [1971], who used a microwave radiometer that was mounted on a fixed ocean platform. Subsequent studies and experiments include a two-scale scattering model [*Dinnat et al.*, 2003], the Wind and Salinity Experiment (WISE), which was part of the prelaunch campaign for SMOS [*Camps et al.*, 2004; *Etcheto et al.*, 2004], and the airborne Passive-Active L-band Sensor (PALS), which was part of the Aquarius prelaunch efforts [*Yueh et al.*, 2010]. More recently, the L-band emissivity was analyzed using brightness temperature observations from the SMOS sensor [*Guimbard et al*., 2012; *Yin et al*., 2012] and for the Aquarius instrument using the Combined Active-Passive (CAP) approach [*Yueh et al*., 2013; *Fore et al*., 2014]. Our study should be regarded as complementary to those earlier analyses. All of our results are based on actual Aquarius observations. Several components of our L-band emissivity model functions based on preliminary data analyses have been presented in *Meissner et al*. [2012a, 2012b].

Most studies agree that an uncertainty in surface wind speed of 1 m/s translates at the Aquarius Earth incidence angles into an uncertainty in the surface brightness temperature of roughly 1/3 K for both vertical and horizontal polarizations. This, in turn, would correspond to an error in the retrieved Aquarius SSS of roughly 2/3 psu for average surface temperatures. This poses a very stringent requirement not only for the accuracy of the wind speed that is used in calculating the roughness signal but also requires an accurate knowledge of the GMF itself.

In order to aid the performance of the removal of the surface roughness emissivity signal, it was decided to combine the Aquarius radiometer with an L-band scatterometer that takes observations at 1.26 GHz simultaneously with the passive instrument [*Yueh et al*., 2012]. The idea is that the active radar observations can provide a characterization of the rough ocean surface at L-band, which is sufficiently accurate to be used in removing the roughness signal from the passive emissivity signal [*Isoguchi and Shimada*, 2009; *Yueh et al*., 2010]. As we will show, the L-band scatterometer observations do not only serve as an accurate proxy for the ocean surface wind speed at the instance and location of the radiometer observation but can also give information on surface roughness that goes beyond wind speed.

The goal of our study is twofold: first, we want to develop an active and passive L-band GMF, which allows an accurate measurement of the ocean surface wind speed. This wind speed will then serve as crucial input for removing the roughness effect in the passive emissivity signal. We will show that in order to do that it is not only essential to have simultaneous active and passive observations but it is also necessary to combine the various channels of the radiometer and scatterometer in an optimal way during the multiple stages of the roughness correction algorithm. We will demonstrate that the wind speed product that we derive for our roughness correction is of excellent quality itself, its accuracy being comparable to wind speeds from validated spaceborne microwave sensor, such as WindSat or SSMIS.

Our analysis is based on a global match-up set of Aquarius brightness temperature (TB) and backscatter (σ_0) measurements that are collocated with wind speed measurements from WindSat and F17 SSMIS.

The GMF for the wind-induced surface emissivity and the form of the surface roughness correction is used in the salinity retrieval algorithm of the Aquarius Version 3.0 data, which has been released by the Aquarius Data Processing System (ADPS) on 9 June 2014 (http://aquarius.nasa.gov/).

Our paper is organized as follow: section 2 describes the features of the match-up data consisting of Aquarius TB and σ_0 observations and WindSat and F17 SSMIS wind speeds and discusses the quality checks that were used to obtain it. We also list and briefly describe the major ancillary fields that we need in our analysis. In section 3, we derive the GMF for the radar backscatter σ_0, and in section 4, we develop the GMF of the wind-induced ocean surface emissivity for the Aquarius channels. Both GMF are functions of surface wind speed and surface wind direction. Section 5 discusses the retrieval and validation of the L-band wind speeds including high wind speeds in tropical and extratropical cyclones. In section 6, we develop the full surface roughness correction model, which is based on this L-band wind speed. We also give an estimate of the accuracy of this roughness correction. In section 7, we compare our model function and wind speed retrievals with the results of other approaches, in particular, the SMOS GMF and the GMF and wind speeds of the CAP algorithm. A summary and conclusions are presented in section 8.

2. Data Sets and Analysis Method

2.1. Aquarius Radiometer and Scatterometer Observations

Our analysis and derivation of the GMF are based on the Aquarius Level 2 (L2) product. It consists of radiometer antenna temperatures (T_A) and radar backscatter measurements σ_0 at the top of the atmosphere (TOA) that are both sampled into 1.44 s time intervals. The Aquarius instrument has three separate feedhorns, each of which taking Earth observations at fixed off-nadir and azimuthal looks. This is known as pushbroom design [*Lagerloef et al*., 2008]. The nominal Earth incidence angles (EIA) of these three horns are 29.36°

(horn 1), 38.44° (horn 2), and 46.29° (horn 3). These values are slightly different from the prelaunch values [*Dinnat and Le Vine*, 2007] because of pointing adjustments that were made postlaunch. The 3 dB footprint averages of along and cross-track directions are 84 km (horn 1), 102 km (horn 2), and 126 km (horn 3). The Aquarius radiometer measure vertical (V-pol) and horizontal (H-pol) polarization as well as the third Stokes parameter (U). The Aquarius scatterometer measures the backscatter σ_0 for co-pol (VV and HH) and cross-pol (VH and HV) channels.

In order to obtain the brightness temperature $T_{B\ surf}$ and radar backscatter σ_0 at the Earth's surface, many spurious signals have to be removed. This is part of the L2 processing algorithms for the radiometer [*Le Vine et al*., 2011; *Wentz et al*., 2012] and the scatterometer [*Yueh et al*., 2012]. The most important of these signals are:

1. Radio frequency interference (RFI) [*Misra and Ruf*, 2008].
2. Cross-polarization contamination in the antenna.
3. Intruding radiation from cold space (spillover).
4. Intruding radiation from celestial sources (galaxy, moon, sun), which can enter the antenna directly from the backlobes or through reflection at the Earth's surface.
5. Faraday rotation in the Earth's ionosphere.
6. For the radiometer measurement, we also need to correct for attenuation in the Earth's atmosphere. For the scatterometer measurements, the atmospheric attenuation can be neglected at L-band frequencies.

The passive GMF will be given in terms of ocean surface emissivity E, which is related to ocean surface brightness temperature by $T_{B\ surf} = E \cdot T_S$, where T_S denotes the sea surface temperature (SST). In this paper, all emissivity values are multiplied by a typical value of $T_S = 290$ K and therefore have units of Kelvin.

The L2 processing for the radiometer is complicated by the fact that the internal Aquarius calibration system exhibits a temporal drift that needs to be corrected before meaningful TB measurements can be obtained [*Piepmeier et al*., 2013]. The basic idea in performing this calibration drift correction is to match the Aquarius salinity product on a global, weekly average with the reference salinity field from the Hybrid Coordinate Ocean Model HYCOM (cf. section 2.4). This matching is done at the TB level. The TB measured from Aquarius are globally matched to the TB that are computed from the geophysical model using the HYCOM SSS.

2.2. Aquarius—Imager Match-Up Data Set: Collocation and Quality Control

For the derivation of the radar backscatter and surface emissivity GMF, we have created a match-up data set of Aquarius $T_{B\ surf}$ and σ_0 observations and microwave imager wind speeds W from the Level 3 (L3) Remote Sensing Systems (RSS) Version 7 climate data record (www.remss.com). For a valid match up, we demand that there exists a wind speed measurement from either WindSat or F17 SSMIS no more than 1 h from the Aquarius observation and that the center of the Aquarius footprint falls within the 1/4° by 1/4° cell of the L3 imager wind speed map. Because all three sensors (Aquarius, WindSat, F17 SSMIS) have approximately the same ascending node times (18:00), the choice of this time window guarantees good global coverage at both low and high latitudes. The mismatch between observation time and resolution of the three sensors will show up in a random sampling mismatch error, which will be part of our validation and error analysis (section 5.3). Decreasing the time window will compromise the global coverage. Increasing the time window will lead to increased mismatch errors.

An observation is discarded if any of the following quality control (Q/C) conditions applies:

1. The land or ice fraction within the Aquarius footprint weighted by the antenna pattern exceeds 0.001. The corresponding estimated uncertainty of land contamination on TA is 0.1–0.15 K if no land correction was included. A first-order land correction is applied in the Level 2 processing.
2. The L2 Aquarius data product flags the scatterometer observation for RFI [*Yueh et al*., 2012].
3. The L2 Aquarius data product indicates possible RFI contamination of the radiometer [*Misra and Ruf*, 2008]. This is the case if the difference between RFI filtered and nonfiltered TA exceeds 0.3 K.
4. The radiometer observation falls within an area for which data analysis indicates that they are likely contaminated by undetected RFI entering through the antenna sidelobes.

5. The L2 Aquarius data product indicates degraded navigation accuracy, or if there is an ongoing spacecraft cold space maneuver or a maintenance maneuver.
6. The RSS L3 map of the imager indicates rain within the 1/4° by 1/4° grid cell or any of its eight surrounding 1/4° by 1/4° grid cells.
7. For the wind speed validation study (section 5.3), we also exclude events if the Ku-band microwave radiometer (MWR) on board the SAC-D spacecraft [*Biswas et al*., 2012] shows rain at the instance of the Aquarius observation. For doing this check, the MWR measurements have been collocated with Aquarius.
8. The value for the average of V-pol and H-pol of the galactic radiation that is reflected from a specular ocean surface exceeds 1.8 K if the wind speed is less than 3 m/s or 2.8 K for any wind speed.

The thresholds that were chosen for items 1, 3, 8 and the regions of suspected undetected RFI (item 4) are based on the results of the degradation study by *Meissner* [2014]. The V3.0 Aquarius L2 files contain explicit Q/C flags, which indicate to the user that the performance starts to degrade in these cases.

Following this match-up procedure, we can create an Aquarius-WindSat and an Aquarius-F17 SSMIS data set. For the derivation of the GMF (sections 3, 4, and 6), we have combined the WindSat and SSMIS sets. If there is a valid match-up wind speed for both WindSat and F17 SSMIS, then we include only the WindSat observation in the match-up set. The time frame that is used in creating this match-up set comprises the full calendar year 2012. The total number of match ups is about 5 million for each of the three Aquarius horns. For the validation of the Aquarius wind speed product in section 5.3, we have used 2 years worth of data comprising September 2011 to August 2013, and we use the Aquarius-WindSat match-up set only. The WindSat wind speeds are slightly more accurate than the F17 SSMIS wind speeds.

Both passive and active GMF depend on wind direction $\varphi_r = \varphi_w - \alpha$ relative to the azimuthal look α, where φ_w is the geographical wind direction relative to North. An upwind observation has $\varphi_r = 0°$, a downwind observation has $\varphi_r = 180°$, and cross-wind observations have $\varphi_r = \pm 90°$. The value for φ_w comes from the ancillary NCEP GDAS field (cf. section 2.4).

For the derivation of the GMF we have averaged the values of E and σ_0 of match-up data set into two-dimensional intervals (W, φ_r), whose sizes are 1 m/s for W and 10° for φ_r.

2.3. Aquarius—Buoy Match Ups

For the wind speed validation in section 5.3, we have created a match-up set of Aquarius observations with wind speed measurements from a global data set of about 200 moored buoys. The data sources for the buoys are the U.S. National Data Buoy Center (NDBC), the Canadian Marine Environmental Data Service (MEDS), the Tropical Atmospheric Ocean TAO/TRITON array (Pacific Ocean), the Pilot Research Moored Array in the Tropical Atlantic PIRATA (Atlantic Ocean), and the Research Moored Array for African-Asian-Australian Monsoon Analysis RAMA (Indian Ocean). The buoy wind speed measurements were referenced to 10 m above the ocean surface. For creating a match up, a buoy observation is used if it is located within the Aquarius 3 dB footprint and if the time of the buoy measurement falls within 60 min of the Aquarius observation.

Most of these buoys are in the tropics but the NDBC and Canadian MEDS buoys guarantee sufficient coverage also at higher northern latitudes reaching up to 55°N. Unfortunately, there are no buoy observations at mid and high southern latitudes and the wind speed range in the buoy match-up set with sufficient valid observations is limited to below 15 m/s.

2.4. Ancillary Geophysical Fields

At various stages of our study, we will use a variety of ancillary fields. These are:

1. Wind speed W_{NCEP} and wind direction $\varphi_{w,NCEP}$ from NCEP GDAS given at a 1° spatial and 6 h temporal resolution. Our data source is ftpprd.ncep.noaa.gov/pub/data/nccf/com/gfs/prod/gdas.YYYYMMDD/gdas1.tHHz.pgrbf00, where YYYY, MM, DD, and HH stand for year, month, day of month, and hour, respectively.
2. Daily SSS from the Hybrid Coordinate Ocean Model HYCOM (www.hycom.org) that were resampled on a 1/4° by 1/4° map. Our data source is ftp.podaac.jpl.nasa.gov (user: aqst, directory/Ancillary/HYCOM/).
3. Daily SST analysis maps from the National Oceanic Atmospheric Administration (NOAA), which are based on measurements from the infrared AVHRR (Advanced Very High-Resolution Radiometer) instrument and

in situ measurements and which were optimally interpolated onto a 1/4° by 1/4° Earth grid [*Reynolds and Smith*, 1994]. Our data source is ftp://eclipse.ncdc.noaa.gov/pub/OI-daily-v2/IEEE/YYYY/AVHRR-AMSR, where YYYY is the year 2002 to present.

4. Significant wave height (WH) data from the NOAA/NCEP Wave Watch III model. Our data source is http://polar.ncep.noaa.gov/waves/download.shtml.
5. The monthly SSS climatology from the 1998 World Ocean Atlas (WOA98, N.O.D.C., CD-ROM).

All of these ancillary fields are linearly interpolated in space and time to the center of the Aquarius footprint and its measurement time. The auxiliary fields 1–4 in the list above are all contained in the Aquarius V3.0 L2 files.

For the validation of Aquarius wind speeds in storms in section 5.4, we also use wind speed analysis fields from NOAA's Hurricane Research Division of Atlantic Oceanographic and Meteorological Laboratory (HRD) [*Powell et al*., 1998]. The data source is http://www.aoml.noaa.gov/hrd/index.html. The HRD wind speed fields have been shifted along the storm track to the time of the Aquarius pass over the storm and resampled to the Aquarius footprint resolution.

2.5. Ionospheric Electron Content and Faraday Rotation

The derivation of the third Stokes ocean surface emissivity signal U in section 4.3 is largely based on maps for the total electron content (TEC) and Faraday rotation in the Earth's ionosphere [*Rybicki and Lightman*, 1979; *Yueh*, 2000; *Le Vine and Abraham*, 2002]. We use TEC maps from the International GPS Service for Geodynamics (IGS). Our data source for this product is ftp://cddis.gsfc.nasa.gov/pub/gps/products/ionex. It contains the vertically integrated electron content between the Earth's surface and an altitude of about 20,200 km. This value needs to be scaled to the altitude of the SAC-D spacecraft, whose average value is 657 km. Our scaling factor is 0.75, which is an average global value based on a model of vertical ionospheric electron density profiles (International Reference Ionosphere IRI 2012, http://irimodel.org/). Using the small-shell approximation [*Klobuchar*, 1987; *Mannucci et al*., 1998], which assumes that the vertical integrated electron content is concentrated in a narrow shell at the mean altitude of the ionosphere, the Faraday rotation angle ψ_F is given by:

$$\psi_F \approx \frac{1.35493 \cdot 10^{-5}}{\nu^2} \cdot (0.75 \cdot \mathrm{TEC}) \cdot (-\mathbf{b} \cdot \mathbf{B}) \cdot \frac{\partial b}{\partial h} \tag{1}$$

In this equation, ν is the frequency of the radiation (in GHz), TEC is given in TECU $= 10^{-16}$ m^2, **B** is the Earth magnetic field vector (in nanotesla) at the mean height of the ionosphere (420 km), **b** is the boresight unit vector from the instrument to the Earth, and the last term is the partial derivative of slant range to the vertical height, which converts TEC to a vertically integrated value to a slant-range integrated value. The values for the Earth magnetic field **B** are taken from the International Geomagnetic Reference Field IGRF 11 (http://www.ngdc.noaa.gov/IAGA/vmod/igrf.html).

3. Radar Backscatter From the Wind Roughened Ocean Surface

The microwave backscatter from rough ocean surface is mainly caused by Bragg scattering from small surface capillary waves that are in equilibrium with the surface wind stress. The GMF of the L-band radar backscatter σ_0 can be expanded into a Fourier series of even harmonic functions in the relative wind direction φ_r [*Wentz*, 1991; *Isoguchi and Shimada*, 2009; *Yueh et al*., 2010]. We keep terms up to second order:

$$\sigma_{0,p}(W, \varphi_r) = B_{0,p}(W) + B_{1,p}(W) \cdot \cos(\varphi_r) + B_{2,p}(W) \cdot \cos(2 \cdot \varphi_r) \tag{2}$$

The harmonic coefficients $B_{k,p}$, k = 0, 1, 2, depend on surface wind speed W, polarization p = VV, HH, VH, HV, and EIA. Using our match-up data set (section 2), we regress the σ_0 measurements to the set of even harmonic basis functions (1; cos(φ_r); cos(2·φ_r)) in each of the 1 m/s wide wind speed bins. The results for $B_{k,p}$, k = 0, 1, 2, and p = VV, HH, VH, HV in each bin are then fitted by a fifth-order polynomial in W, which vanishes at W = 0:

$$B_{k,p}(W) = \sum_{i=1}^{5} b_{ki,p} \cdot W^i \tag{3}$$

The values of the coefficients $b_{ki,p}$ for the three Aquarius horns and polarizations VV, HH, and VH are listed in file ts01.txt in the supporting information. The cross-pol channels VH and HV are assumed to be identical in

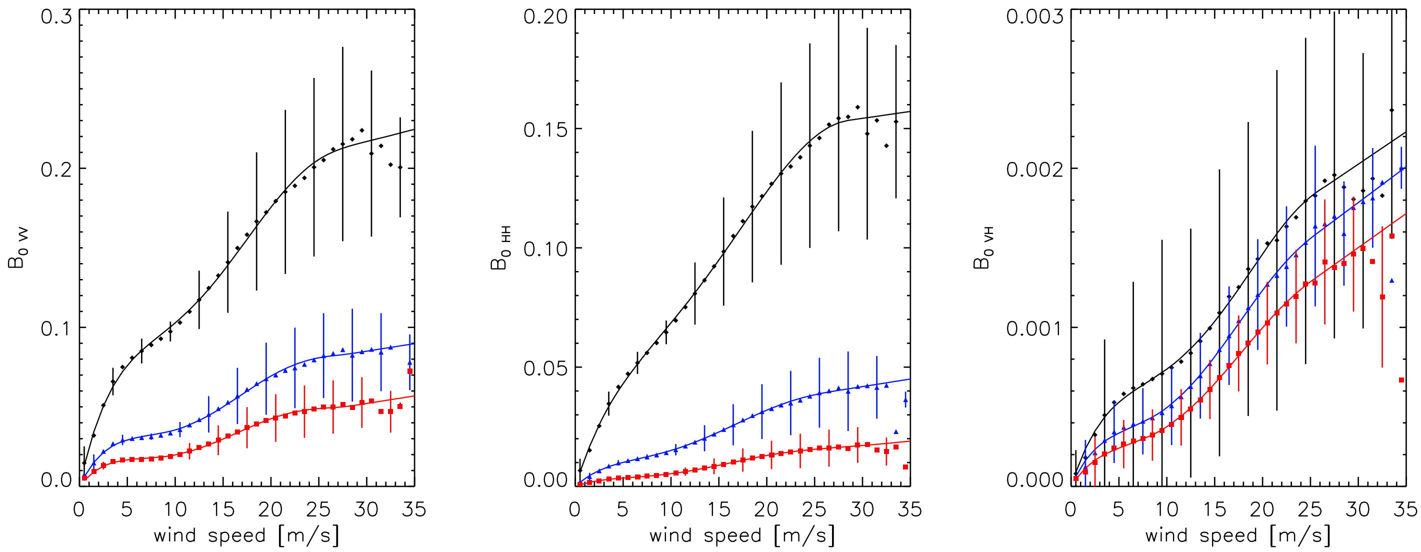

Figure 1. The zeroth harmonic B_0 of the scatterometer GMF as function of wind speed for the channels (left) VV, (middle) HH, and (right) VH. The Aquarius data are indicated by black diamonds for horn 1, blue triangles for horn 2, and red squares for horn 3. The full lines are the fifth-order polynomial fits. For readability, the error bars are shown only at every third data point.

the Aquarius TOA σ_0. The wind speed dependence of the harmonic coefficient $B_{0,p}(W)$ is displayed in Figure 1. Figure 2 shows the wind direction dependence of $\sigma_{0,p}$ at three different wind speeds: 6.5, 10.5, and 14.5 m/s.

Several interesting results can be seen from these figures. For VV and HH, all three harmonic coefficients loose sensitivity to wind speed at high winds ($W > 20$ m/s). This behavior was also observed with the radar backscatter GMF at higher frequencies: C-band [*Hersbach et al.*, 2007] and Ku-band [*Wentz and Smith*, 1999; *Ricciardulli and Wentz*, 2011]. The cross-pol channel VH seems to keep sensitivity to wind speeds even above 25 m/s. In our GMF, we linearly extrapolate $B_{0,p}$ if $W > 28$ m/s and $B_{1,p}$ and $B_{2,p}$ if $W > 22$ m/s. We also see from Figure 2 that the wind directional signal is very small below 8 m/s. Actually, the figure indicates that at lower wind speeds this small directional signal of VV and HH has an opposite sign than at higher wind speeds. This observation agrees with the results of the PALSAR (Phased-Array L-Band Synthetic Aperture Radar) campaign [*Isoguchi and Shimada*, 2009]. On the other hand, such a behavior of the directional signal is not evident in either the C-band nor the Ku-band GMF, which both show a significant directional backscatter signal down to at least 5 m/s and the signal has the same sign at all

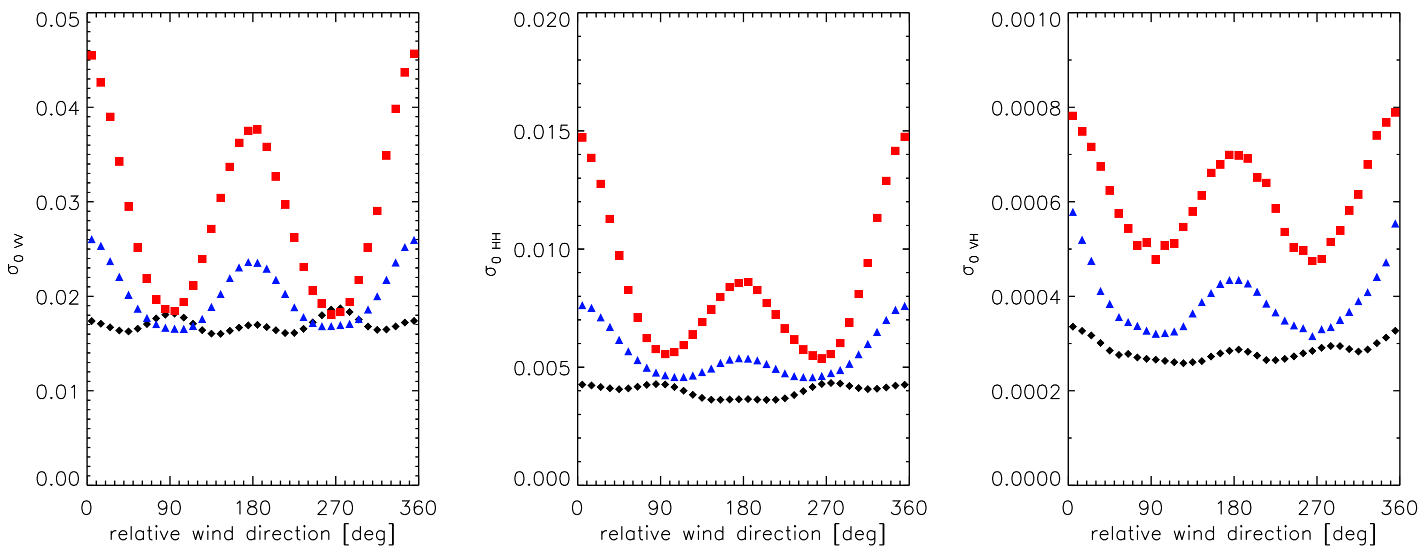

Figure 2. The wind direction dependence of the scatterometer cross section σ_0 of Aquarius horn 3 channels (left) VV, (middle) HH, and (right) VH at three different wind speeds: 6.5 m/s (black diamonds), 10.5 m/s (blue triangles), 14.5 m/s (red squares).

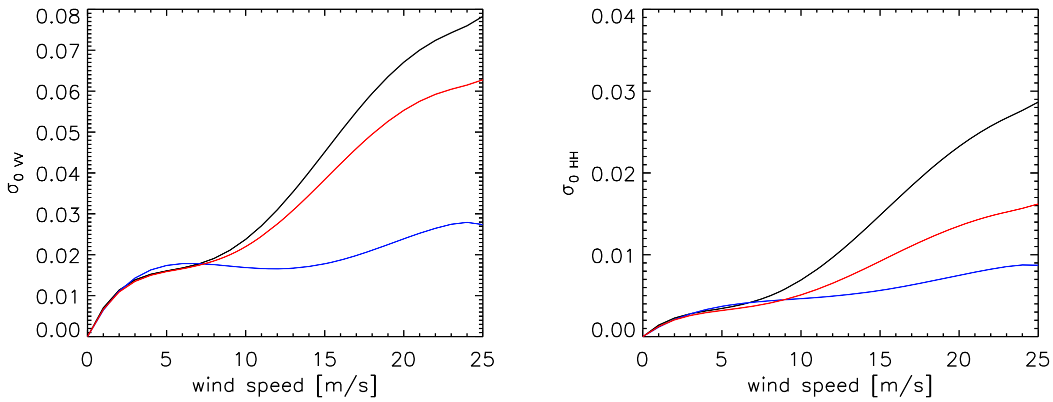

Figure 3. Scatterometer GMF of Aquarius horn 3 channels (left) VV and (right) HH: up-wind (black), cross wind (blue), and down-wind (red).

wind speeds. At this point, it is not clear what causes this behavior of the L-band directional signal at low winds.

Another important feature, in which the radar backscatter at L-band differs noticeably from the higher frequencies (C-band, Ku-band) and which is not yet understood, shows up in Figure 3, which displays the total backscatter $\sigma_{0,p}$ for VV and HH as function of wind speed for upwind ($\varphi_r = 0°$), downwind ($\varphi_r = 180°$), and cross-wind ($\varphi_r = 90°$) observations. Above 5 m/s, the cross-wind signal completely loses sensitivity to wind speed. The VV-pol σ_0 even becomes nonmonotonic with increasing W.

The sensitivity loss to wind speed of the L-band σ_0 at high wind speeds and for cross-wind observations will become important for measuring wind speeds from L-band radar observations, which we will discuss in detail in section 5.

4. Emission From the Wind Roughened Ocean Surface

4.1. Emission From the Specular Ocean Surface

At a given frequency, the surface emissivity E can be modeled with a specular part E_0 and a part caused by ocean roughness ΔE_{rough}:

$$E = E_0(T_S, S, \theta) + \Delta E_{rough} \tag{4}$$

The emissivity of the specular ocean surface E_0 is by far the largest part. It depends on sea surface temperature T_S, sea surface salinity S, EIA θ, and polarization p = V, H. E_0 is determined by the complex dielectric constant (permittivity) of seawater ε through the Fresnel equations:

$$\begin{gathered} E_{0,p} = 1 - |r_p|^2, \quad p = V/H-\text{pol} \\ r_V = \frac{\varepsilon(T_S, S)\cdot\cos(\theta) - \sqrt{\varepsilon(T_S,S) - \sin^2(\theta)}}{\varepsilon(T_S, S)\cdot\cos(\theta) + \sqrt{\varepsilon(T_S,S) - \sin^2(\theta)}} \qquad r_H = \frac{\cos(\theta) - \sqrt{\varepsilon(T_S,S) - \sin^2(\theta)}}{\cos(\theta) + \sqrt{\varepsilon(T_S,S) - \sin^2(\theta)}} \end{gathered} \tag{5}$$

Meissner and Wentz [2004] provided a fit for ε, which was based on modeling the frequency dependence through a double Debye relaxation law. An ensemble of weighted data from laboratory measurements and SSM/I observations was used in order to fit the Debye relaxation parameters by minimizing the total error between observations and model. A minor update of this fit for ε was done in *Meissner and Wentz* [2012] by incorporating results from WindSat measurements at C-band and X-band. This is the dielectric model that we have used for this study with two small amendments, which we would like to mention here: there is a typo in the sign of the parameter d_3 in *Meissner and Wentz* [2012, Table 7]. The correct value is $d_3 = -0.35594 \times 10^{-6}$. In addition, the T_S dependence of the second Debye relaxation frequency ν_2 in *Meissner and Wentz* [2004, equation (17)] had been changed from $b_{10}\cdot T_S$ to $b_{10}\cdot(T_S + 30°C)/2$. This change has already been used in *Meissner and Wentz* [2012], but it was not listed. It should be noted that no Aquarius measurements have been used in the development of the dielectric model.

In order to compute $E_{0,p}$ (T_S, S) in the derivation of the GMF for the wind-induced ocean surface emissivity, we use the ancillary HYCOM SSS field as described in section 2. The important assumption is that when taking long-term global averages there is no crosstalk error between the HYCOM SSS ancillary fields and wind speed W. Such a crosstalk error could introduce a spurious signal in the GMF. The validity of that assumption has been tested by comparing HYCOM SSS with in situ buoy measurements from the ARGO network, indicating no noticeable systematic correlation between HYCOM-buoy SSS and wind speed [*Lagerloef and Kao*, 2013]. It has also been justified a posteriori by comparing Aquarius SSS, which is using our roughness correction algorithm, with SSS from ARGO drifters, showing again no noticeable correlation between Aquarius-ARGO SSS and wind speed [*Abe and Ebuchi*, 2013].

4.2. Wind-Induced Emissivity for V-Pol and H-Pol

In general, the ocean surface emissivity is influenced by wind speed through three different mechanisms:

1. Large gravity waves, whose wavelengths are long compared with the radiation wavelength. These large-scale waves mix vertical and horizontal polarizations and change the local incidence angle of the electromagnetic radiation. This mechanism is described by the geometric optics approach.
2. Small gravity-capillary waves, which are riding on top of the large-scale waves and whose RMS height is small compared with the radiation wavelength. These small-scale waves cause diffraction (Bragg scattering) of radiation that is backscattered from the ocean surface. From Kirchhoff's law it follows that they also affect the passive microwave emission of the sea surface.
3. Sea foam, which arises as a mixture of air and water at the wind roughened ocean surface and which leads to a general increase in the surface emissivity. This effect becomes dominant at high wind speeds at C-band and higher frequencies [*Monahan and O'Muircheartaigh*, 1980].

The emissivity signal that is produced by these mechanisms is largely isotropic, which means it is independent on relative wind direction φ_r. However, processes 1 and 2 give rise to small anisotropic contributions, which cause a dependence on φ_r.

According to equation (4), the roughness signal ΔE_{rough} is computed by subtracting the specular surface emissivity E_0 from the measured value of the total emissivity E in the match-up data set.

As a first step in the GMF derivation, we parameterize ΔE_{rough} as function of wind speed W, relative wind direction φ_r, and SST T_S: $\Delta E_{rough} = \Delta E_{W0}$ (W, φ_r, T_S). For the full roughness correction in section 6, we will also add scatterometer observations and significant wave height data into the model function for ΔE_{rough}.

Meissner and Wentz [2012] found that for higher-frequencies (C-band and above) ΔE_{rough} is approximately proportional to the specular surface emissivity E_0. This can be understood within the geometric optics approach by the fact that the wind roughened surface mixes the vertical and horizontal polarizations of the specular surface and the mixing increases with increasing emissivity of the specular surface. We follow the same approach at L-band and model the SST dependence of ΔE_{rough} as:

$$\Delta E_{W0,p} = \delta_p(W, \varphi_r) \cdot \frac{E_{0,p}(T_S)}{E_{0,p}(T_{ref})} \qquad T_{ref} = 20^\circ C \tag{6}$$

Figure 4 shows that this behavior is indeed approximately correct for SST values between 0°C and 25°C: the decrease of ΔE_{W0} (squares in the right plot) with increasing T_S is similar to the decrease of E_0 (left) in this temperature interval and the ratio $\Delta E_{W0}/E_0$ (triangles) stays approximately constant. One can see from the Figure 4 (left) that over the whole dynamic range of ocean SST (0°C–30°C), the value of E_0 of the Aquarius channels changes by about 10%. One should note that we have not considered any dependence on salinity in (6) despite the fact that the L-band emissivity is sensitive to salinity. Over the whole dynamic range of ocean salinity (30–40 psu), the value of E_0 of the Aquarius channels changes only by about 4%. Figure 4 also shows that at very high SST the ansatz in equation (6) becomes less accurate. One reason for this might be that the HYCOM reference SSS, which is used in the computation of E_0, does not fully capture the freshening due to rain in tropical regions [*Boutin et al*., 2013] and therefore slightly overestimates the salinity. The consequence is an underestimate of the value for E_0 and thus a slight overestimate of the value for ΔE_{W0}, which is evident in Figure 4. Another reason could be that the ansatz (6) itself breaks down at high SST. As stated, it is based on the geometric optics approach and at L-band other mechanisms such as Bragg

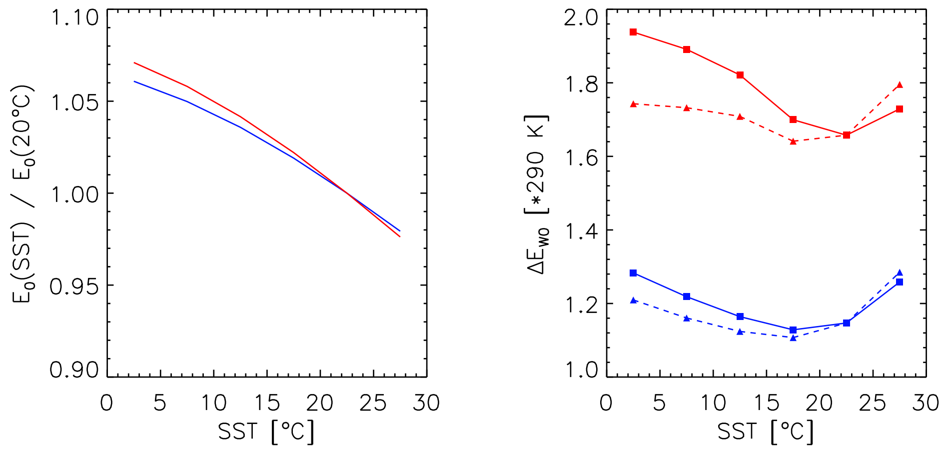

Figure 4. (left) The value of the form factor δ (specular emissivity relative to its value at $T_{ref} = 20°C$) of Aquarius horn 3 as function of SST. (right) The wind-induced emissivity averaged over a representative sample of wind speeds as function of SST. The full lines/squares are the Aquarius data. The dashed lines/triangles are the Aquarius data after dividing by the form factor δ. The blue graphs are for V-pol. The red graphs are for H-pol after shifting by −1.0 K for readability. The values have been multiplied by a common surface temperature of 290 K.

scattering become important. This issue needs to be kept in mind to account for possible errors in the retrieved Aquarius salinity at higher SST. Overall, as Figure 4 shows, introducing the SST dependence according to (6) is an improvement over assuming no SST dependence in ΔE_{W0}.

The model function for the form factor δ is again an even second-order harmonic expansion:

$$\delta_p(W, \varphi_r) = A_{0,p}(W) + A_{1,p}(W) \cdot \cos(\varphi_r) + A_{2,p}(W) \cdot \cos(2 \cdot \varphi_r) \quad (7)$$

The harmonic coefficients $A_{k,p}$, $k = 0, 1, 2$, depend on surface wind speed W, polarization $p = V, H$, and EIA. We follow the same procedure as for the derivation of the L-band radar backscatter GMF. The values for $\delta_p = \Delta E_{W0,p}/E_{0,p}$ are regressed to the set of even harmonic basis functions (1; $\cos(\varphi_r)$; $\cos(2\cdot\varphi_r)$) in each of the 1 m/s wide wind speed bins. The results for $A_{k,p}$, $k = 0, 1, 2$ in each bin are then again fitted by a fifth-order polynomial in W, which vanishes at $W = 0$:

$$A_{k,p}(W) = \sum_{i=1}^{5} a_{ki,p} \cdot W^i \quad (8)$$

File ts02.txt in the supporting information lists the values of the coefficients a_{ki} for the three Aquarius horns and the V-pol and H-pol polarizations. The wind speed dependence of the three harmonic coefficients $A_{k,p}$ (W), $k = 0, 1, 2$, $p = V, H$ are plotted in Figure 5 for V-pol and in Figure 6 for H-pol. For computing the error bars in A_0, we use the standard deviation of the measurements of ΔE_W in each wind speed bin. The error bars for the higher harmonics A_1 and A_2 are the residuals of the harmonic fit (7).

One important feature that is obvious from Figures 5 and 6 is the linear rise at high wind speeds of the isotropic part $A_{0,p}$, which is by far the largest term in the wind-induced emissivity ΔE_{W0}. In contrast to the radar backscatter GMF, which starts to saturate above 25 m/s, the wind-induced emissivity keeps good sensitivity even at very high wind speeds. The good sensitivity of the emissivity at high wind speeds has also been observed at SMOS [*Reul et al.*, 2012]. It is due to the emission from foam covered ocean surface, which becomes the dominant mechanism in the surface emission at higher wind speeds. The same behaviors are observed in the GMF for both emissivity [*Meissner and Wentz*, 2012] and radar backscatter [*Hersbach et al.*, 2007; *Ricciardulli and Wentz*, 2011; *Meissner et al.*, 2011b] at higher frequencies. Another difference between emissivity and radar backscatter GMF is that there is no sensitivity loss of ΔE_{W0} to wind speed at cross-wind observations. This can be seen from Figures 5 and 6, as the magnitude of the isotropic part A_0 is much larger than the one of the higher harmonics A_1 and A_2, which depend on wind direction. Thus, the impact of wind direction on the total value (7) is small. Both of these differences between passive and active L-band sensors will become important in section 5 for the measurement of L-band wind speeds.

The curves in Figures 5 and 6 suggest to linearly extrapolate the wind speed dependence of $A_{0,p}$ (W) and to keep the values of $A_{1,p}$ (W) and $A_{2,p}$ (W) constant if $W > 25$ m/s.

10.1002/2014JC009837

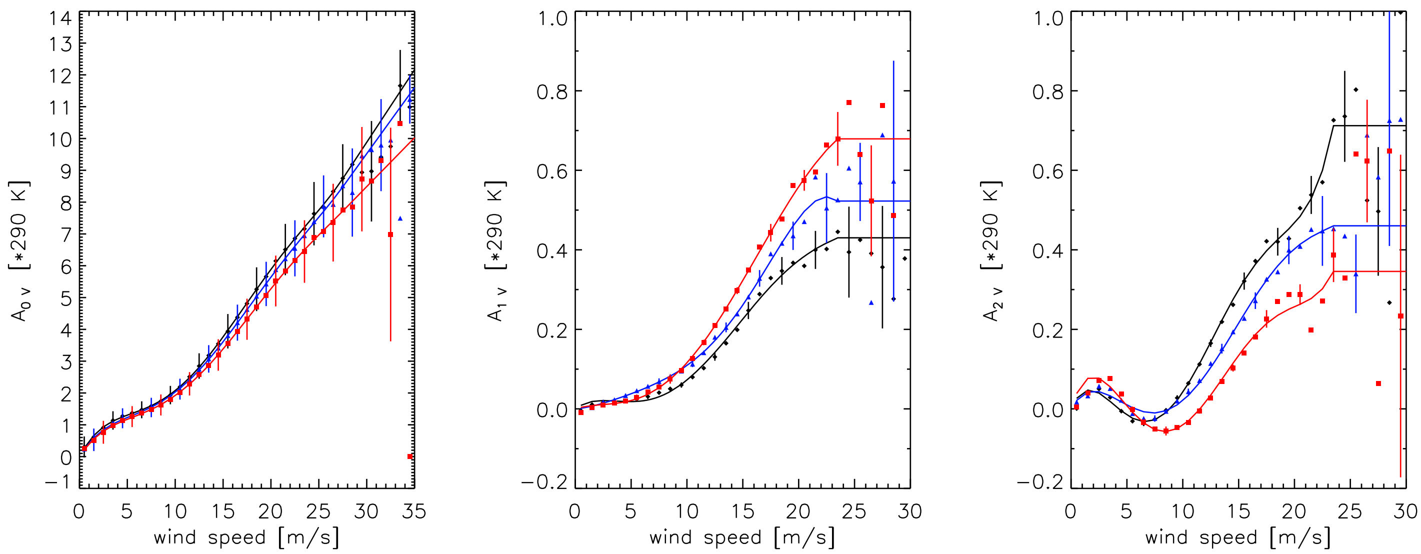

Figure 5. The harmonic coefficients A_k, k = 0, 1, 2, of the wind-induced emissivity GMF as function of wind speed for V-pol. The values have been multiplied by a common surface temperature of 290 K. The Aquarius data are indicated by black diamonds for horn 1, blue triangles for horn 2, and red squares for horn 3. The full lines are the fifth-order polynomial fits. For readability, the error bars are shown only at every third data point.

Figure 7 shows the directional signal of ΔE_{W0} at three different wind speeds: 6.5, 10.5, and 14.5 m/s. The signal is small below 8 m/s. At the high incidence angle (horn 3), the first harmonic A_1 dominates the V-pol signal whereas the second harmonic A_2 dominates the H-pol signal, as it is the case at higher frequencies [*Meissner and Wentz*, 2002, 2012]. The small second harmonic A_2 at low wind speeds has the opposite sign than at high wind speeds. This behavior is similar to what we have already observed for the L-band radar backscatter GMF in section 3. This feature has so far only been observed at L-band and the physical mechanism of its s cause is not yet understood. Above 8 m/s, the directional signal in all three horns becomes sizeable for both polarizations and it is important to remove it from the observation in order to meet the accuracy requirement of 0.2 psu in the SSS measurement.

Finally, we want to note that the Aquarius measurements allow the derivation of a GMF at the EIA of the three Aquarius horns. The interpolation procedure of *Meissner and Wentz* [2012] can be used to extend it to other EIA values.

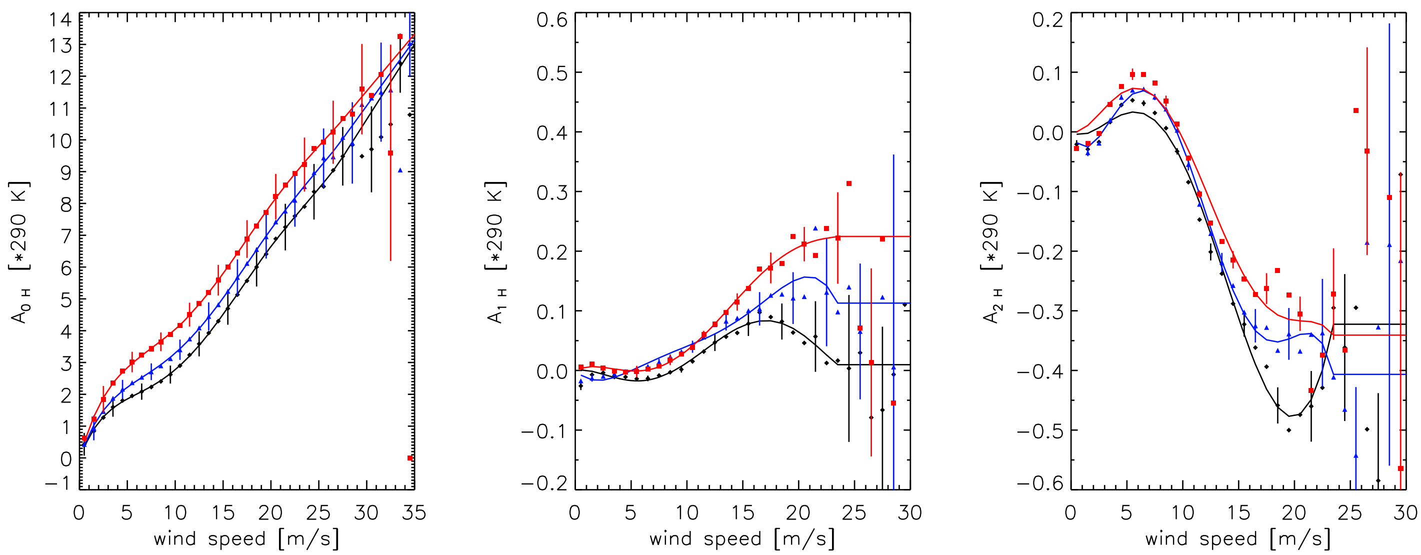

Figure 6. The harmonic coefficients A_k, k = 0, 1, 2 (from left to right), of the wind-induced emissivity GMF as function of wind speed for H-pol. The values have been multiplied by a common surface temperature of 290 K. The Aquarius data are indicated by black diamonds for horn 1, blue triangles for horn 2, and red squares for horn 3. The full lines are the fifth-order polynomial fits. For readability, the error bars are shown only at every third data point.

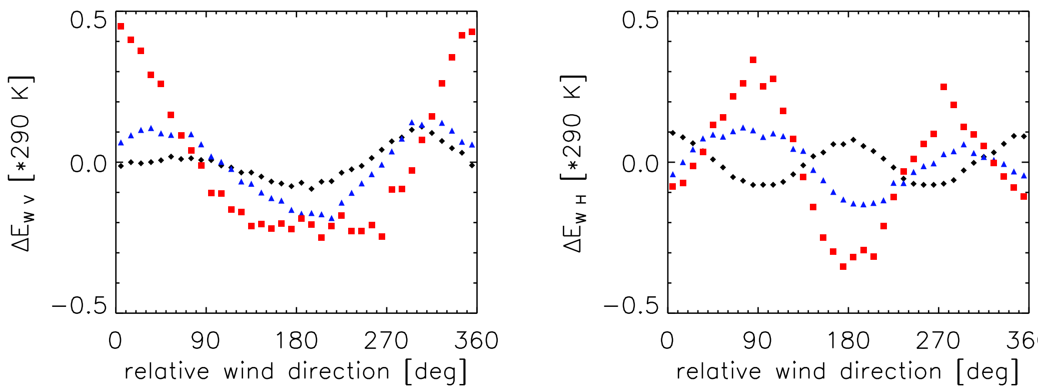

Figure 7. The wind direction dependence of the wind-induced emissivity ΔE_W of Aquarius horn 3 (left) V-pol and (right) H-pol at three different wind speeds: 6.5 m/s (black diamonds), 10.5 m/s (blue triangles), and 14.5 m/s (red squares). The values have been multiplied by a common surface temperature of 290 K and the isotropic part A_0 has been subtracted.

4.3. Wind Direction Signal of the Third Stokes Parameter

In addition to V-pol and H-pol, the Aquarius radiometer measures the third Stokes parameter U. The main purpose of doing this is to have the ability to accurately correct for the rotation ψ of the electromagnetic polarization basis between Earth observation point and antenna. This polarization rotation ψ has two components $\psi = \psi_{ion} + \psi_{geo}$:

1. The Faraday rotation ψ_{ion}, which actively rotates the electromagnetic polarization vector when traveling from the top of the atmosphere (TOA) to the top of the ionosphere (TOI).

2. The passive geometric polarization rotation ψ_{geo} between Earth and antenna polarization basis vectors [*Meissner and Wentz*, 2006; *Dinnat and Le Vine*, 2007; *Piepmeier et al.*, 2008; *Meissner et al.*, 2011a].

The ionospheric part ψ_{ion} scales with the inverse square of the frequency. In case of Aquarius, this means that its size amounts to about 80–90% of the total polarization rotation angle ψ assuming the spacecraft flies at or near it nominal attitude.

The polarization rotation mixes the second Stokes $Q = T_{BV} - T_{BH}$ and the third Stokes parameter U according to:

$$\begin{pmatrix} Q \\ U \end{pmatrix}_{TOI} = \begin{bmatrix} \cos(2\psi) & -\sin(2\psi) \\ +\sin(2\psi) & \cos(2\psi) \end{bmatrix} \cdot \begin{pmatrix} Q \\ U \end{pmatrix}_{TOA} \tag{9}$$

Equation (9) implies that:

$$Q_{TOI}{}^2 + U_{TOI}{}^2 = Q_{TOA}{}^2 + U_{TOA}{}^2 \tag{10}$$

The TOI TB values are obtained from the measured antenna temperatures after removing cross-polarization contamination in the antenna and correcting for intrusion of celestial radiation (cold space, galaxy, sun, moon) into the Aquarius field of view [*Wentz et al.*, 2012]. The TOA TB for Q and U are related to their surface values after correcting for atmospheric attenuation [*Wentz et al.*, 2012]. This means in particular that $U_{TOA} \approx \tau^2\, U_{surf}$. τ is the value for the atmospheric transmittance [*Meissner and Wentz*, 2012], which is very close to 1.

The Aquarius salinity retrieval algorithm [*Wentz et al.*, 2012] assumes that there is no third Stokes surface signal ($U_{surf} = U_{TOA} = 0$). Equation (10) allows then the retrieval of the TOA second Stokes Q_{TOA} from the measurements Q_{TOI} and U_{TOI} and thus for an accurate correction of the polarization basis rotation. On the other hand, if a value for the rotation angle $\psi = \psi_{ion} + \psi_{geo}$ is available, which is independent of the Aquarius measurement, it can be used together with the measurements for Q_{TOI} and U_{TOI} to obtain a prediction for U_{TOA} and thus for the surface third Stokes U_{surf}. The small geometric part ψ_{geo} of the rotation angle can be computed from the pointing geometry [*Meissner and Wentz*, 2006; *Meissner et al.*, 2011a]. The large ionospheric part ψ_{ion} (Faraday rotation) can be predicted from ancillary maps of the ionospheric TEC, as explained in section 2.5.

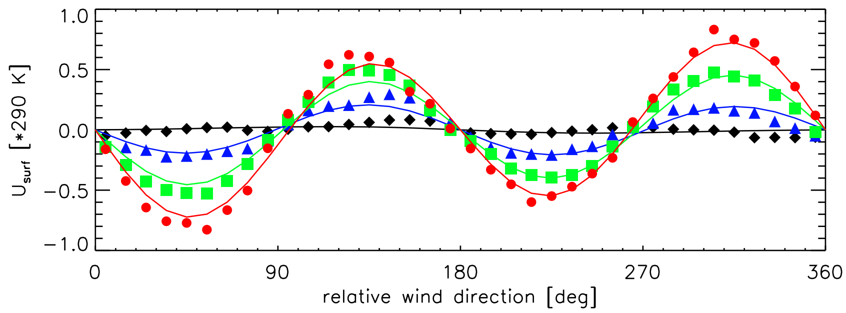

Figure 8. The wind direction dependence of the third Stokes parameters U at the ocean surface U_{surf} of Aquarius horn 1 at four different wind speeds: 7.5 m/s (black diamonds), 10.5 m/s (blue triangles), 13.5 m/s (green squares), and 16.5 m/s (red circles). The symbols indicate the Aquarius data and the full lines the second-order harmonic fit of equation (11). The values have been multiplied by a common surface temperature of 290 K.

Figure 8 shows the directional signal U_{surf} for Aquarius horn 1 that is obtained this way at four different wind speeds: 7.5, 10.5, 13.5, and 16.5 m/s. Below 7.5 m/s the surface third Stokes is indeed very small, which justifies the assumption of the Aquarius salinity retrieval algorithm to neglect it. However, at higher wind speed, the third Stokes surface signal becomes sizeable. Though the data are noisy, which is mainly due to the uncertainties in the TEC maps and the knowledge of the scaling factor (section 2.5), the expected odd harmonic signal clearly shows up:

$$U_{surf} = A_{1,U}(W) \cdot \sin(\varphi_r) + A_{2,U}(W) \cdot \sin(2 \cdot \varphi_r) \tag{11}$$

The harmonic coefficients increase with wind speed and at 16.5 m/s the peak-to-peak amplitude of the third Stokes signal reaches ± 1.5 K for horn 1. We find that the size of this signal decreases for the higher incidence angles. Compared to horn 1, the peak to peak amplitude is about 80% for horn 2 and 45% for horn 3.

5. Wind Speed Retrievals From Combined Passive and Active Observations

5.1. Maximum Likelihood Estimation (MLE)

We use the GMF for the radar backscatter cross section σ_0 and the wind-induced surface emissivity ΔE_{W0} that we have derived in sections 3 and 4, respectively, to estimate Aquarius ocean surface wind speeds. The Aquarius wind speed retrieval algorithm is a MLE minimizing the weighted sum of square differences between the Aquarius observations and the GMF. For this study, we consider two Aquarius wind speed products:

1. A wind speed based on scatterometer HH-pol observations, which we call HH wind.
2. A wind speed based on scatterometer HH-pol and radiometer H-pol observations, which we call HHH wind.

The MLE for the HH wind speed retrieval algorithm is:

$$\chi^2_{HH}(W) = \frac{\left[\sigma^{measured}_{0,HH} - \sigma^{GMF}_{0,HH}(W, \varphi_r)\right]^2}{\mathrm{var}\left(\sigma_{0,HH}\right)} + \frac{\left[W - W_{NCEP}\right]^2}{\mathrm{var}\left(W_{NCEP}\right)} \tag{12}$$

The MLE for the HHH wind speed retrieval algorithm is:

$$\chi^2_{HHH}(W) = \frac{\left[\sigma^{measured}_{0,HH} - \sigma^{GMF}_{0,HH}(W, \varphi_r)\right]^2}{\mathrm{var}\left(\sigma_{0,HH}\right)} + \frac{\left[T^{measured}_{B,surf,H} - T^{GMF}_{B,surf,H}(W, \varphi_r)\right]^2}{\mathrm{var}\left(T_{B,surf,H}\right)} + \frac{\left[W - W_{NCEP}\right]^2}{\mathrm{var}\left(W_{NCEP}\right)} \tag{13}$$

In both cases, the wind direction is obtained from the ancillary NCEP GDAS field (section 2.4).

The combination of simultaneous active and passive observations for wind speed measurements has already been studied with the SEASAT scatterometer (SASS)-radiometer (SMMR) system [*Moore et al.*, 1982] and recently applied to Aquarius [*Yueh and Chaubell*, 2012; *Yueh et al.*, 2013]. At L-band frequencies, the inclusion of radiometer observations into the wind speed retrieval improves the skill at high wind speeds and for cross-wind observations in which the scatterometer starts loosing sensitivity to wind speed, as we have discussed in section 3.

The HH-wind, though less accurate than the HHH wind at higher wind speeds, becomes useful if a wind speed is needed at the stages of the salinity retrieval algorithm in which calibrated radiometer TB are not yet available. This is the case in the calibration drift correction [*Piepmeier et al.*, 2013] or the removal of celestial radiation (galaxy, sun) that gets reflected from the ocean surface [*Wentz et al.*, 2012].

The poor sensitivity of the radar backscatter σ_{0HH} at cross-wind observations (Figure 2), which has already been mentioned in section 3, makes it necessary to use an auxiliary field. Therefore, we are assimilating the NCEP wind speed W_{NCEP} as background field into the HH MLE (12) for the HH wind speed algorithm. As a consequence, the algorithm will converge to this background field at cross wind. The HHH wind algorithm does not need the auxiliary field, as the H-pol emissivity does not show the cross-wind sensitivity loss. Nevertheless, we have decided to use W_{NCEP} as background field in the HHH MLE (13) as well.

In order to compute the radiometer H-pol GMF in the HHH wind speed retrieval algorithm, we need an ancillary first-guess fields for SSS. One possibility is to take a climatology salinity field (e.g., from the World Ocean Atlas WOA) or a model (e.g., HYCOM). It is also possible to do the HHH wind speed retrieval iteratively. In a first step, one retrieves HH wind speed, which uses scatterometer observations only and therefore does not need any ancillary input SSS. In the second step, one uses this HH wind speed to retrieve SSS. The final step is to take this SSS as ancillary input in the HHH wind algorithm.

5.2. Determination of Channel Weights

The various terms in the MLE of equations (12)–(13) are weighted by their inverse estimated variances, which are the squares of the estimated errors. Our estimated errors include instrument noise, knowledge errors in the instrument parameters (e.g., EIA), uncertainties in the GMF, and errors in the ancillary fields that are used in the GMF (e.g., SST and SSS). In order to calculate these estimated errors, we have computed the standard deviations of the difference between measured and GMF value for σ_0 and ΔE_{W0} in our match-up data set. In case of the background field W_{NCEP}, we take the standard deviation between W_{NCEP} and the imager wind speed. All of these estimated error values contain the error from the imager wind speed and the sampling mismatch between imager and Aquarius observation. This contribution should not be included in MLE weights, as it is neither related to the Aquarius measurement nor the GMF and it therefore needs to be backed out in a root sum square sense from the standard deviation. We have allocated a total error of $\Delta W = 0.6$ m/s for the uncertainty in the imager wind speed and the sampling mismatch error, which is based on validation studies [*Meissner et al.*, 2011b]. The GMF for σ_0 and ΔE_{W0} can be used to translate this value into an equivalent error for σ_0 and ΔE_{W0}. This error is then removed from the standard deviation to give the final values for the channel weights. In the wind speed retrieval algorithm, we need to know a first-guess value for the wind speed in order to look up the value of the estimated error that is tabulated in file ts03.txt in the supporting information, because the tabulated error values depend on wind speed. We are using W_{NCEP} to do that.

We have found that when using these channel weights in the MLE, the inclusion of any of the additional scatterometer channels (VV, VH, and HV) or the V-pol radiometer channel does not lead to further improvement of the retrieved Aquarius wind speed. The VV-pol scatterometer channel contains information on the surface roughness that is orthogonal to the information given by surface wind speed, as we will discuss in sections 6.1 and 6.2. Moreover, as it can be seen from Figure 3, σ_{0VV} becomes not only insensitive but even nonmonotonous as function of wind speed for cross-wind observations, which can introduce multiple local minima in the cost function of the MLE. Section 6 will show that the VV-pol is still useful for the surface roughness correction of the emissivity, but we do not include it in the wind speed retrievals. The signal to noise ratio of the radar cross-pol channels VH and HV is too small to make these channels useful to be included into the MLE. The V-pol radiometer channel is less sensitive to wind speed but more sensitive to SSS than the radiometer H-pol channel. This channel is used in the actual SSS retrieval algorithm [*Wentz et al.*, 2012].

5.3. Performance Estimate of Aquarius Wind Speed Retrievals

In order to assess the accuracy of the Aquarius HH and HHH wind speed products, we have compared them with the WindSat wind speeds of our match-up data set (section 2.2). Figure 9 shows the values for bias and standard deviations stratified as function of WindSat wind speed. For comparison, we have also included

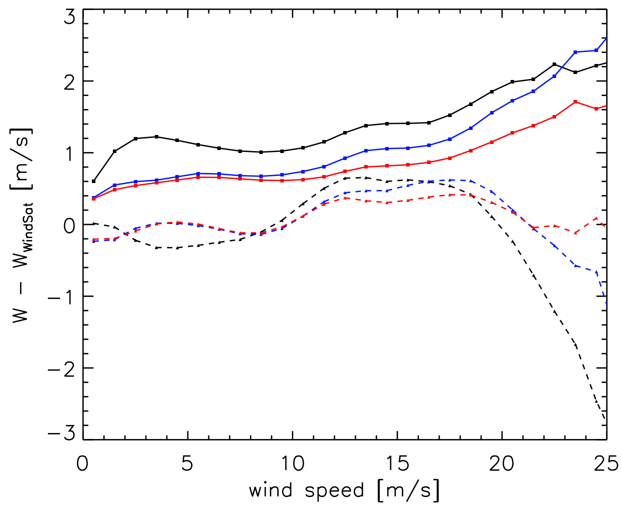

Figure 9. Performance statistics of rain-free Aquarius wind speeds summed over all three horns and stratified with respect to WindSat wind speed. Dashed lines/triangles display the biases and full lines/squares display the standard deviation. The black curves are NCEP GDAS-WindSat wind speeds, the blue curves are Aquarius HH-WindSat wind speeds, and the red curves are Aquarius HHH-WindSat wind speeds. The *x* axis wind speed values are the arithmetic average between WindSat wind speed and Aquarius/NCEP GDAS wind speeds.

the statistic result for NCEP wind speed versus imager wind speed in Figure 9. It can be seen that over the whole wind speed range both HH and HHH wind speeds perform significantly better than NCEP, which is used as a background field in the MLE (section 5.1).

Figure 10 shows the joint probability density function between Aquarius HHH and WindSat wind speeds and Figure 11 between Aquarius and buoy wind speeds from the match-up set that has been described in section 2.3. The black dashed lines in both figures indicate the bias between Aquarius wind speed and the validation wind. Table 1 lists the standard deviations between several Aquarius wind speed products and WindSat.

Figures 9–11 show that no significant systematic wind speed biases exist between Aquarius HHH wind speeds and any of the validation sets below 25 m/s. Unfortunately, very few rain-free Aquarius or validation data exist above 25 m/s. The next section will give a performance estimate of high Aquarius wind speeds based on a study of selected cases.

Figure 9 also shows that for higher wind speeds, the HHH winds perform better than the HH winds. In particular, above 20 m/s, the HH wind performance starts to degrade. This is expected, because, as discussed in sections 3 and 4, the radar backscatter GMF starts loosing sensitivity at higher wind speeds whereas the wind-induced emissivity does not. Below 8 m/s the performance of scatterometer only (HH) and combined radiometer-scatterometer (HHH) wind speeds are basically identical.

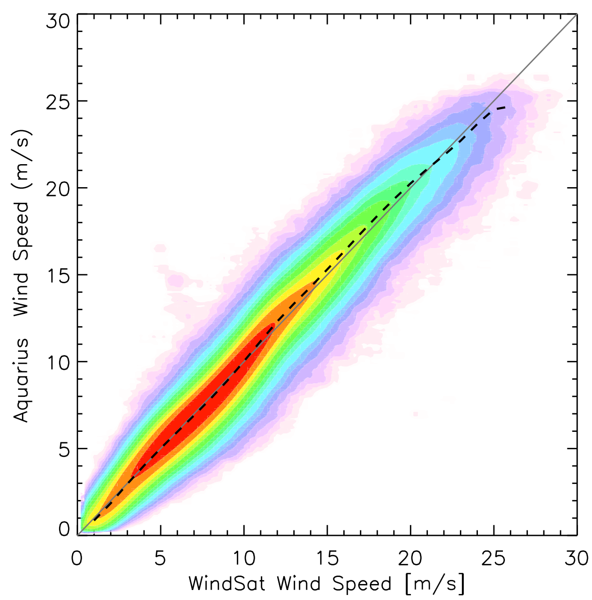

Figure 10. Normalized joint probability distribution function for rain-free Aquarius HHH wind speeds versus collocated WindSat wind speeds. The contour lines are spaced approximately dual logarithmically in order to emphasize the distribution tails. The dashed black line represents the Aquarius-WindSat wind speed bias.

Creating a triple collocation match-up set between Aquarius, WindSat, and buoys allows the computation of the standard deviation of the mutual difference of each pair of the three wind speed data sets at the same observation time and location. This triple collocation match-up set comprises more than 4000 data. The results are listed in the left columns of Table 2. Because the three measurements are independent, the errors of the single measurement σ_i can be computed from the standard deviations of the three mutual differencesσ_{ij}:

$$\sigma_i{}^2 = \frac{1}{2}\left(\sigma_{ij}{}^2 + \sigma_{ik}{}^2 - \sigma_{jk}{}^2\right) \quad i, j, k = 1, 2, 3 \tag{14}$$

The results of the triple collocation analysis of Aquarius HHH, WindSat, and buoy wind speeds are listed in the right columns of Table 2. It should be kept in mind that the Aquarius observations have the lowest resolution

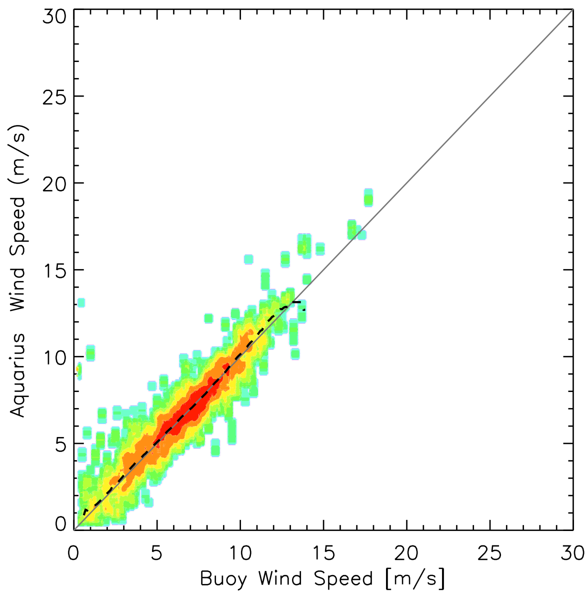

Figure 11. Normalized joint probability distribution function for rain-free Aquarius HHH wind speeds versus collocated buoy wind speeds. The contour lines are spaced approximately dual logarithmically in order to emphasize the distribution tails. The dashed black line represents the Aquarius-buoy wind speed bias.

(100–150 km) compared with WindSat (35 km) and the buoys (point observation). The error figure for the buoys in Table 2 is largely dominated by sampling mismatch between the different resolutions. Nevertheless, these results demonstrate that the quality of the Aquarius wind speed at its 100 km resolution matches the quality of the wind speed products from the two imager instruments (WindSat, SSMIS) and that from the QuikSCAT [*Ricciardulli and Wentz*, 2011; *Meissner et al.*, 2011b] and ASCAT [*Verspeek et al.*, 2010] scatterometers.

The probability density functions for the wind speed distributions of the Aquarius-WindSat match ups are shown in Figure 12 and for the Aquarius-buoy match ups in Figure 13. There is very good agreement between Aquarius HHH and the WindSat and buoy pdf. As expected, the half width of the Aquarius HHH wind distribution is slightly smaller than the one of WindSat and the buoys because the Aquarius winds have a lower resolution. The NCEP GDAS distribution, which is also shown in Figure 12, is shifted slightly toward lower wind speeds. This feature is prevalent when comparing NCEP GDAS wind speeds with satellite-derived wind speeds and has already been observed in other studies [*Meissner et al.*, 2001].

5.4. Aquarius Wind Speeds in Storms

The capability of L-band radiometers to measure wind speed in hurricanes has been demonstrated by *Reul et al.* [2012] for SMOS. We conclude our validation of the Aquarius HH and HHH wind speeds with a brief look at their performance in storms with strong winds and intense rain. Figure 14 shows the time series of the along-track cross section of one of the Aquarius horns through the center of three storms: one tropical cyclone (hurricane Katia, left plot) and two extratropical cyclones (center and right plots). In the first case, we use HRD wind fields (section 2.4) and in the latter two cases the RSS WindSat all-weather wind speed [*Meissner and Wentz*, 2009] for comparison. In all three cases, we have turned off the rain-flagging that has been applied as Q/C in the construction of the match-up set (section 2.2), and therefore the cases shown in Figure 14 do contain rain. Collocated imager rain rates from WindSat [*Hilburn and Wentz*, 2008] are available for the last two cases and plotted as red lines. The HHH wind speeds match very well the reference, HRD or WindSat all-weather winds, even in winds as high as 40 m/s and in intense rain. The HH wind speed becomes inaccurate above 25 m/s, which is again likely due to the sensitivity loss of the scatterometer GMF at high winds. The results indicate that combined L-band scatterometer and radiometer wind speed might be usable in strong storms and even if rain is present. We should caution, however, as a systematic study of the rain effect at L-band is still outstanding. While the atmospheric attenuation at L-band frequencies is very small even in rain [*Wentz*, 2005], it is not clear if and how rain splashing at the ocean surface can have an impact on the surface roughness and on the quality of the retrieved wind speeds [*Weissman et al.*, 2012; *Boutin et al.*, 2013].

Table 1. Standard Deviation (in m/s) of Differences Between Various Aquarius L-Band Wind Speed Products (HHH, HH, CAP Version 2.5.1) and WindSat Wind Speeds

Wind Speed Products	Σ
Aquarius HHH–WindSat	0.70
Aquarius HH-WindSat	0.80
Aquarius CAP-WindSat	0.93

6. Surface Roughness Correction for the Aquarius Ocean Salinity Retrieval Algorithm

6.1. Full Model Function for the Radiometer Surface Roughness Correction

The full model function for the roughness correction of the Aquarius surface brightness temperature also

Table 2. Triple Collocation: Aquarius HHH, WindSat, Buoy Wind Speeds[a]

Wind Speed Product Differences	Σ	Individual Wind Speed Product	σ
Aquarius HHH-WindSat	0.61	Aquarius HHH	0.42
Aquarius HHH-Buoy	1.06	WindSat	0.44
Buoy-WindSat	1.07	Buoy	0.97

[a]The left side shows the standard deviation of the mutual differences. The right side shows the errors of the individual products estimated from the triple collocation method. All units are m/s.

includes scatterometer VV-pol and WH (wave height) observations. As we will see in section 6.4, this leads to a small but noticeable improvement in the accuracy of the roughness correction and thus in the accuracy of the SSS. We write the model function as a sum of three terms, whose size and importance decrease with ascending order:

$$\Delta E_{rough} = \Delta E_{W0}(W, \varphi_r, T_S) + \Delta E_{W1}\left(W, \sigma'_{0,VV}\right) + \Delta E_{W2}(W, WH). \quad (15)$$

For the wind speed, we use the HHH wind in all three terms. The largest (zeroth order) term in this sum is ΔE_{W0} (W, φ_r, T_S), which is the wind-induced emissivity GMF that we have derived and discussed in section 4.

The next-to-leading order term ΔE_{W1} (W, $\sigma'_{0,VV}$) is a two-dimensional lookup table that depends on HHH wind speed and the measurement of the VV-pol radar cross section after removing the wind direction signal according to equation (2).

$$\sigma'_{0,VV} \equiv \sigma_{0,VV}^{meas} - \left[B_{1,VV}(W_{NCEP}) \cdot \cos(\varphi_r) + B_{2,VV}(W_{NCEP}) \cdot \cos(2 \cdot \varphi_r)\right]. \quad (16)$$

The scatterometer VV-pol has not been used in the retrieval of the Aquarius wind speed and can therefore contain additional valuable information for the surface roughness correction. In order to derive the lookup table ΔE_{W1}, we compute the residuals between the observation for the wind-induced surface emissivity and the GMF ΔE_{W0} (W, φ_r, T_S) and average it into equal two-dimensional [W, $\sigma'_{0,VV}$] intervals. The result is displayed in Figure 15 for horn 3. For visual reasons, we have linearly scaled the units of the cross section into equivalent wind speeds. This scaling is based on the GMF values for $B_{0,VV}$ (W) in section 3. The left plot in Figure 15 contains the population density of each [W, $\sigma'_{0,VV}$] interval. The middle plot shows ΔE_{W1} for the V-pol, and the right plot for the H-pol. The V-pol ΔE_{W1} is small over most of the [W, $\sigma'_{0,VV}$]-region. However, the H-pol ΔE_{W1} is sizeable both in the case of high winds relative to small $\sigma'_{0,VV}$ as well as small winds relative to large $\sigma'_{0,VV}$. Its absolute value exceeds 0.4 K in those regions of the [W, $\sigma'_{0,VV}$] diagram. That shows that the VV-pol radar measurement contains indeed additional valuable information on the surface roughness that is not contained in the Aquarius HHH wind speed.

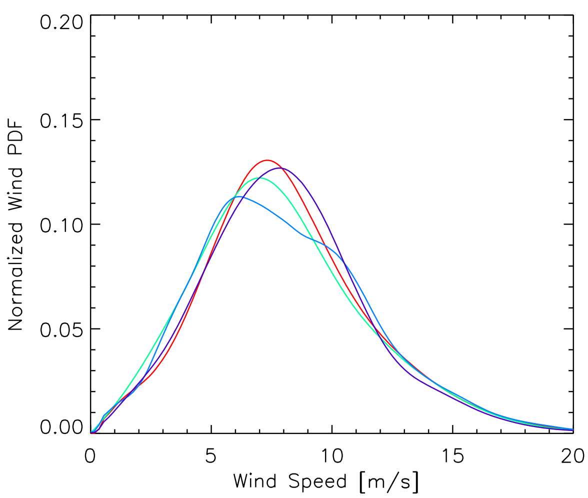

Figure 12. Probability distribution function (in s/m) of rain-free Aquarius HHH wind speeds (red line) collocated with WindSat (purple), CAP Version 2.5.1 (light blue), and NCEP GDAS (green). The size of the wind speed bins is 0.1 m/s.

Finally, the second-order term ΔE_{W2} (W, WH) in equation (15) is a two-dimensional lookup table depending on wind speed W and wave height WH. The wave height values come from the NOAA/NCEP Wave Watch III model (section 2.4). In order to derive ΔE_{W2} (W, WH), we repeat the procedure above but this time computing the residuals between the observation for the wind-induced surface emissivity and the sum ($\Delta E_{W0} + \Delta E_{W1}$) and bin it into equally spaced [W, WH] intervals. The results for the population density and the values for ΔE_{W2} are shown in Figure 16 for horn 3. We see that most of the surface roughness information is already contained in wind speed and the scatterometer VV-pol measurement and thus in the terms ΔE_{W0} and ΔE_{W1}. Consequently, the dependence of the residuals ΔE_{W2} on WH is weak.

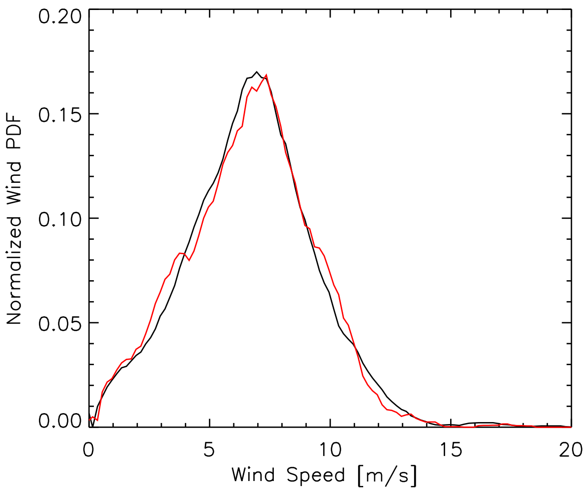

Figure 13. Probability distribution function (in s/m) of rain-free Aquarius HHH winds (red line) collocated with buoys (black). The size of the wind speed bins is 0.1 m/s.

File ts04.txt in the supporting information provides the full lookup tables for ΔE_{W1} (W, $\sigma'_{0,VV}$) and file *ts05.txt* provides the full lookup table for ΔE_{W2} (W, WH). Two-dimensional [W, $\sigma'_{0,VV}$] or [W, WH] intervals with population less than 100 are regarded as underpopulated and the values of ΔE_{W1} or ΔE_{W2} are not used in the roughness correction and they are also not shown in the diagrams of Figure 15 or Figure 16. In those cases, we decided to just take $\Delta E_{rough} = \Delta E_{W0}$.

We need to note that our choice (15) for the form of the roughness correction GMF is by no means unique. For example, one could consider a parameterization for the first-order term that depends on [$\sigma'_{0,VV}$, $\sigma'_{0,HH}$] rather than on [W, $\sigma'_{0,VV}$].

6.2. Dependence on Input Wind Speed

It is also important to point out that the roughness correction GMF does depend on which input wind speed is used. Our GMF (15) and the values for the lookup tables for ΔE_{W1} and ΔE_{W2} are based on HHH wind speeds. For the derivation of $\Delta E_{W0,}$ we had used imager wind speeds from our match-up data set, which, as seen in Figure 9, matches the HHH wind speeds very well. For demonstration, let us now present a case for the roughness correction in which no L-band scatterometer measurements but only ancillary NCEP wind vector and WH fields are available. The residuals between observed wind-induced emissivity and zeroth-order GMF ΔE_{W0} can be written as a two-dimensional lookup table $\Delta E'$ (W_{NCEP}, WH), which is displayed in Figure 17. When comparing it with Figures 15 and 16 it is evident that, if combined with NCEP wind speeds, the WH contains important information on the surface roughness in a similar way as the scatterometer observations do. If W_{NCEP} is used in the roughness correction and if there is no scatterometer measurement available, it is useful to include WH information into the GMF. On the other hand, as we have seen in section 6.1, if WH data are included into the GMF (15) in addition to

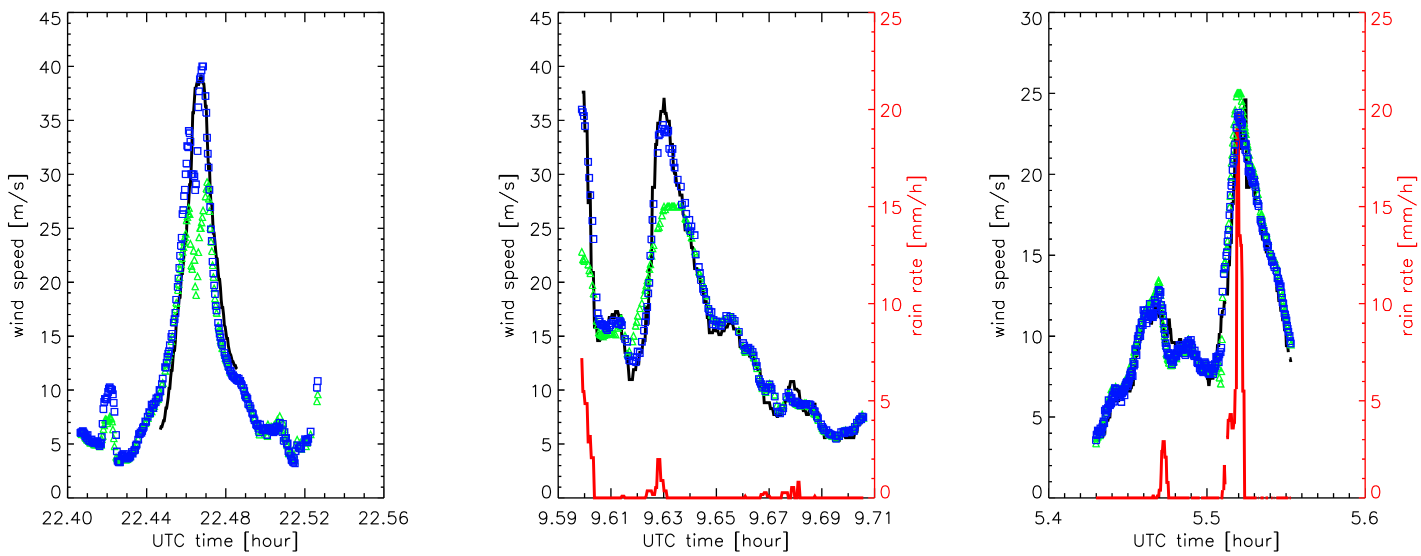

Figure 14. Along-track cross section of rain-free Aquarius HHH (blue squares) and HH (green triangles) wind speeds (in m/s) for three storms: (left) Aquarius horn 2 on 6 September 2011 (Hurricane Katia). The black line is the HRD model wind speed field after shifting it along the storm track to the time of the ascending Aquarius overpass and resampling it to the Aquarius resolution. (middle) Aquarius horn 1 in extratropical cyclone centered near (50°N, 50°W) on 30 November 2012. (right) Aquarius horn 3 in rain intense extratropical cyclone centered near (40°N, 180°W) on 12 April 2013. In the last two cases, the black line in the WindSat all-weather wind speed and the red line is the WindSat surface rain rate (mm/h).

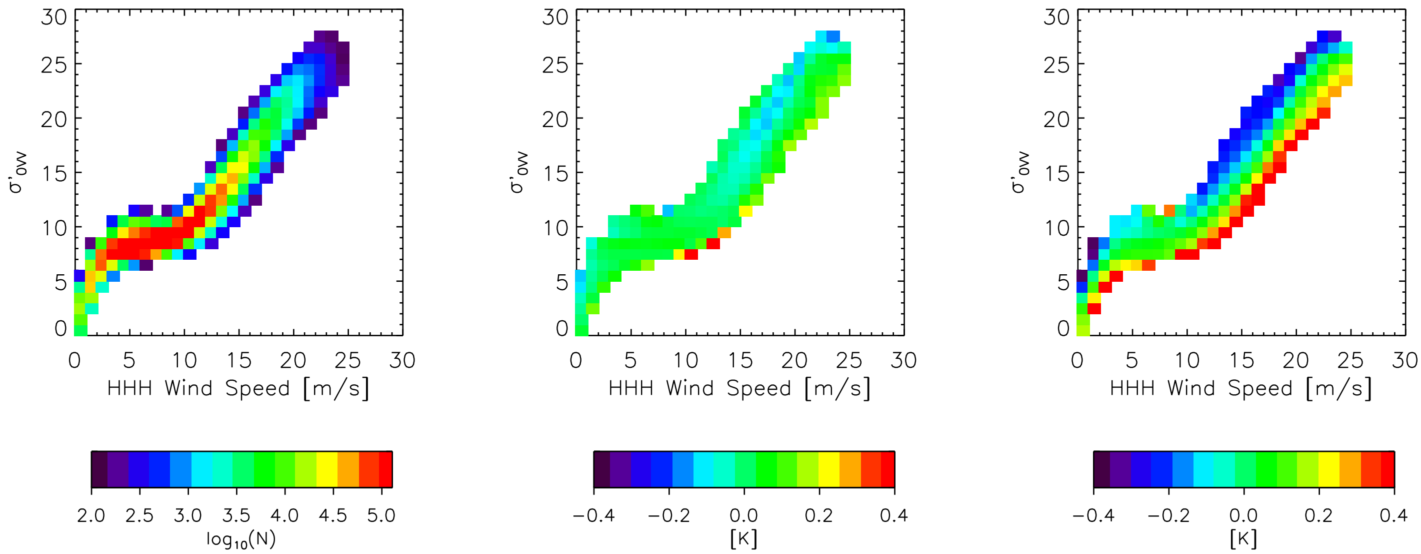

Figure 15. The correction ΔE_1 (W_{HHH}, σ'_{0VV}) to the wind-induced emissivity for Aquarius horn 3. (left) The population density in each [W_{HHH}, σ'_{0VV}] bin, (middle) ΔE_1 for the V-pol emissivity, and (right) ΔE_1 for the H-pol emissivity. The emissivity values have been multiplied by a common surface temperature of 290 K. The σ'_{0VV} denotes the VV scatterometer cross section after removing the wind direction signal. The values of σ'_{0VV} have been scaled to equivalent wind speeds: an interval of 1 m/s of the *y* axis corresponds to a value of $\sigma'_{0VV} = 0.002$ (in real units).

$\sigma_{0,HH}$ and $\sigma_{0,VV}$, the resulting dependence on WH is very weak. Accordingly, the improvement in the accuracy is only marginal. We hope that our results might help to understand this issue sometime in the future within the framework of the theory of scattering and emission of electromagnetic radiation from rough ocean surfaces.

It should also become clear from this discussion that it is important to input the Aquarius HHH wind speed product into equation (15) and into the lookup tables for ΔE_{W1} (W, $\sigma'_{0,VV}$) and ΔE_{W2} (W, WH). Using W_{NCEP} rather than W_{HHH} could result in inaccuracies. Conversely, the lookup table $\Delta E'$ from Figure 17 takes the NCEP wind speeds as input and not the HHH wind speeds.

6.3. Components and Flow of Surface Roughness Correction Algorithm

We are now in a position to put together all the parts of the surface roughness correction for the Aquarius salinity retrieval algorithm. Figure 18 shows a flow diagram with the major components and how they interact. It also exhibits what observations and ancillary data are used during each step.

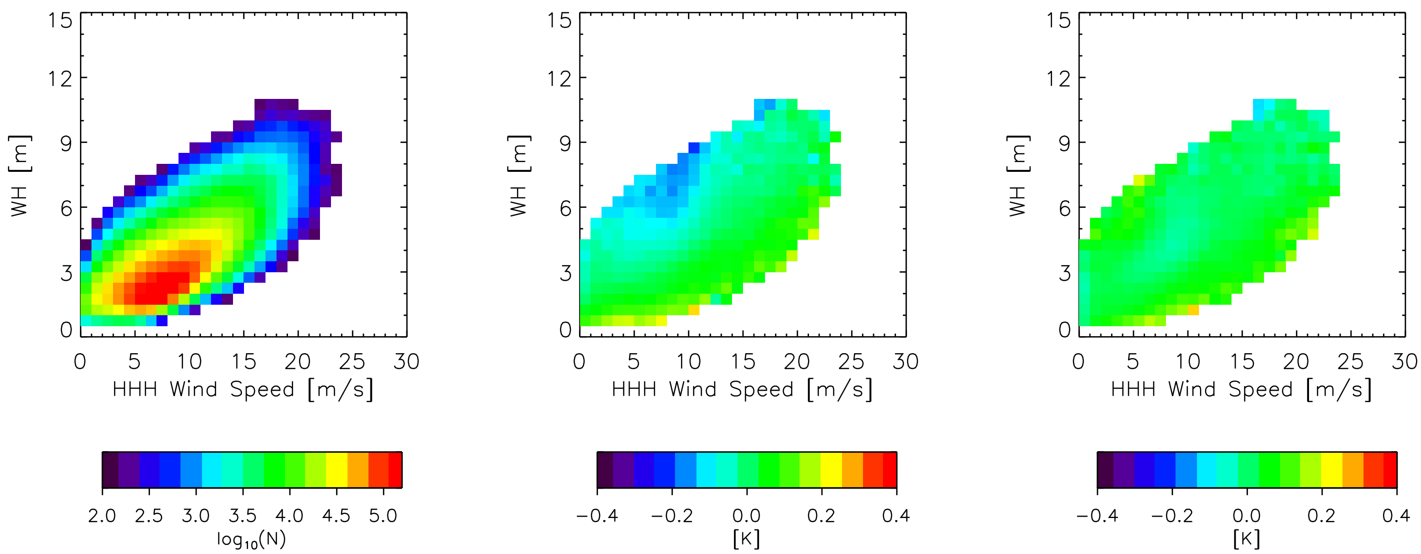

Figure 16. The correction ΔE_2 (W_{HHH}, WH) to the wind-induced emissivity for Aquarius horn 3. (left) The population density in each [W_{HHH}, WH] bin, (middle) ΔE_2 for the V-pol emissivity, and (right) ΔE_2 for the H-pol emissivity. The emissivity values have been multiplied by a common surface temperature of 290 K.

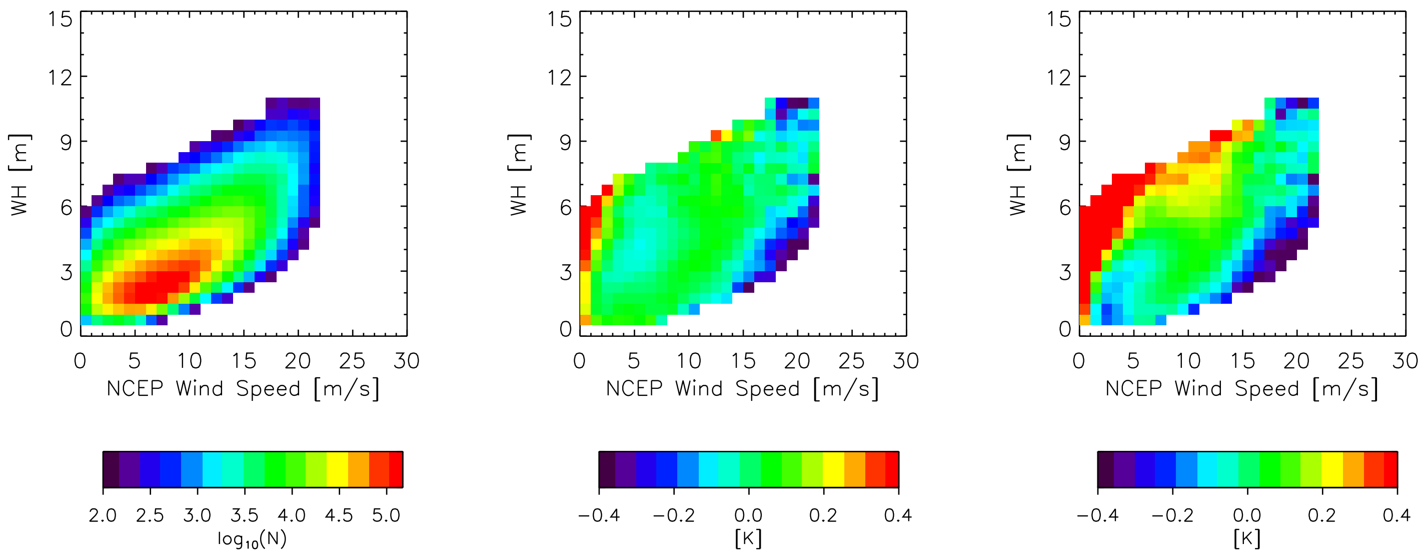

Figure 17. The correction $\Delta E'$ (W_{NCEP}, WH) to the wind-induced emissivity for Aquarius horn 3. (left) The population density in each [W_{NCEP}, WH] bin, (middle) $\Delta E'$ for the V-pol emissivity, and (right) $\Delta E'$ for the H-pol emissivity. The emissivity values have been multiplied by a common surface temperature of 290 K.

6.4. Accuracy of Roughness Correction Algorithm

The accuracy of the surface roughness correction algorithm can be assessed by comparing measured with computed surface brightness temperatures. In the computation, we use the ancillary HYCOM SSS field. The result is presented in Table 3, which lists the RMS difference between measured and computed surface brightness temperatures for the six Aquarius channels. In order to demonstrate the importance of the surface roughness input parameter that is available to perform the correction, we have compared five cases:

1. Ancillary NCEP wind speed and direction only. The surface roughness GMF consists only of the zeroth-order term ΔE_{W0} (W_{NCEP}, φ_r, T_S).
2. WH data in addition to that, which is the case discussed in section 6.2. The GMF contains the additional term $\Delta E'$ (W_{NCEP}, WH).
3. HHH wind speeds, which requires HH-pol scatterometer measurements. The surface roughness GMF consists of the zeroth-order term ΔE_{W0} (W_{HHH}, φ_r, T_S) from equation (15).
4. Scatterometer VV-pol observation in addition to that. The surface roughness GMF is the sum $\Delta E_{W0} + \Delta E_{W1}$ from equation (15).
5. WH data in addition to that. In this case, the surface roughness GMF is the full equation (15).

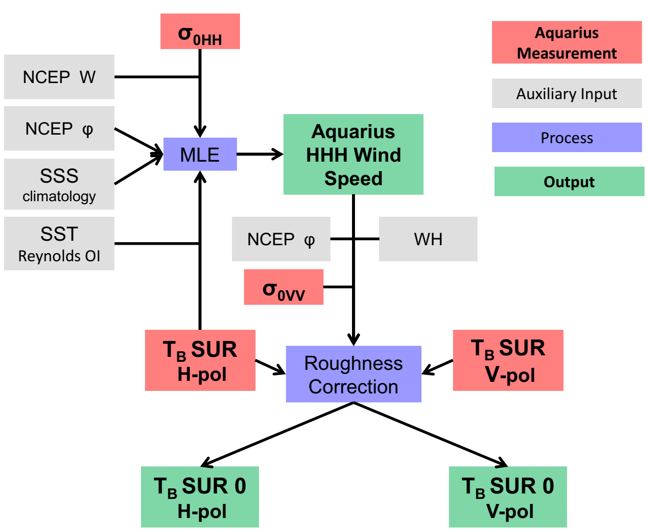

Figure 18. Flow diagram of the Aquarius surface roughness correction algorithm.

The by far largest improvement occurs between the second and the third step with the inclusion of the scatterometer HH-pol observation, which leads to a drop in the RMS error by about 22–29% for the V-pol channels and about 37–45% for the H-pol channels. This demonstrates the importance of the ability to use the scatterometer observations in the roughness correction. It is far superior over having only ancillary numerical weather prediction wind speed fields and WH model data available. In that respect, the Aquarius sensor has a distinct advantage over SMOS [*Font et al*., 2004], which has only an L-band radiometer but no radar on board.

Finally, we should mention that the global accuracy estimate for the RMS between measured and computed surface TB of case 5 in Table 3 translates into a global error for the retrieved Aquarius SSS of approximately 0.50–0.53 psu, based on the translation 1 K (ΔT_B) = 2 psu (ΔSSS), if only V-pol channels are used in the retrievals. This is to be compared to error figures of about 0.71 psu if no scatterometer is used (case 2 in Table 3).

The error figures of case 5 in Table 3 are larger than the requirement of 0.2 psu, but it should be kept in mind that this accuracy value applies to a single 1.44 s observation cycle. Further noise reduction is obtained after averaging the single 1.44 s measurements of the 3 horns into monthly 150 km maps.

7. Comparison With Other Studies

In this section, we compare our L-band GMF and L-band wind speed retrievals with the findings of other previous studies.

Most importantly, we find very good agreement, within the margins of error, between our isotropic wind-induced emissivity A_0 (W) and the corresponding result of the SMOS analysis [*Guimbard et al*., 2012; *Yin et al*., 2012] for winds below 20 m/s. The SMOS study has limited its wind speed range to below 20 m/s. The curves given in *Guimbard et al*. [2012] and *Yin et al*. [2012] were interpolated to the incidence angles of the Aquarius horns in order to compare results. This agreement demonstrates a high level of consistency between the SMOS and Aquarius analyses of wind-induced emissivity, which holds despite the fact that the size of Aquarius footprints (100–150 km) are more than twice as large as SMOS footprints (40 km). Moreover, comparison of Aquarius wind speeds with buoys, which provide a point measurement of wind speed, have revealed no significant biases (section 5.3). This indicates that the GMF of the wind-induced emissivity at L-band has little or no dependence on footprint size and resolution of the sensor.

In another study, the predictions of the two-scale model with the DV2 spectrum [*Dinnat et al*., 2003, 2012] show relatively good agreement with the Aquarius-derived GMF over the wind speed range 2–15 m/s. The RMS between the two-scale model and the Aquarius data is 0.08–0.12 K for the V-pol channels and 0.18–0.25 K for the H-pol channels. In order to compute these numbers, an average bias over the whole wind speed range has been removed in each horn [*Dinnat et al*., 2012]. This bias can reflect an absolute calibration offset in the instrument, which is impossible to determine from the instrument parameters. As explained in section 2.1, the Aquarius TB are matched to the TB computed from the geophysical model over the global ocean.

The prelaunch WISE [*Camps et al*., 2004; *Etcheto et al*., 2004] and PALS [*Yueh et al*., 2010] campaigns have provided model fits for the isotropic part of the wind-induced emissivity model. They have assumed a linear increase of ΔE_W with wind speed. The reason for this assumption was simply a lack of data at higher wind speeds in both campaigns, which did not allow for a more accurate determination of the GMF. At wind speeds below 6 m/s the PALS emissivity agrees well with our GMF for both V-pol and H-pol and so does the WISE emissivity for H-pol. The WISE prediction for the V-pol emissivity is much too small at the middle and outer horns, being almost zero at horn 3. All other studies and measurements show a sizeable V-pol emissivity even at 45° incidence. Because of their assumed linear increase with wind speed, neither the PALS nor the WISE GMF can describe the wind-induced emissivity well enough at wind speeds above 6 m/s to be used in actual salinity retrievals of SMOS or Aquarius.

Earlier versions of our wind emissivity GMF [*Meissner et al*., 2012a, 2012b] were based on only a few months of data compared with the one full year that was used in this study. The reduced data volume results in

Table 3. Performance of Surface Roughness Correction: RMS Difference Between Measured and Computed Surface Brightness Temperatures for the Six Aquarius Channels (in Kelvin)

Input Parameters	1V	1H	2V	2H	3V	3H
NCEP wind speed only	0.362	0.374	0.363	0.396	0.359	0.431
NCEP wind speed + WH	0.356	0.365	0.358	0.385	0.354	0.414
HHH wind speed only	0.253	0.230	0.264	0.220	0.277	0.228
HHH wind speed + σ_{0VV}	0.249	0.211	0.261	0.204	0.272	0.207
HHH wind speed + σ_{0VV} + WH	0.244	0.207	0.256	0.200	0.268	0.205

higher noise especially at higher wind speeds. The previous analysis was not able to give reliable predictions above 18 m/s. The most important difference between our previous work and that reported here concerns the surface roughness correction. The earlier study used NCEP wind speeds whereas the present study uses the Aquarius HHH wind speeds. The significant positive impact of this change to the accuracy of the surface roughness correction is demonstrated in section 6.4.

Due to the strong similarity in the approaches for deriving the L-band wind emissivity and radar GMF we also expect general agreement between the GMF of the CAP algorithm [*Yueh et al*., 2013] and our algorithm, which is used in the ADPS Version 3.0 data release. The most noticeable difference between these two GMFs is the second harmonic coefficient A_2 of the V-pol wind emissivity signal at high incidence angles. While the results for horn 1 agree within the margins of error, our A_2 coefficient for horn 3 is only half the size of the CAP value. Our results for the wind direction signal in the third Stokes parameter U (section 4.3) is about 15–20% smaller than CAP. This lies within the margins of error.

There are, however, more noticeable discrepancies between CAP and our algorithm when it comes to retrieving wind speed and using the winds in the surface roughness correction of the salinity retrieval. The most important differences are the combinations of scatterometer and radiometer channels that both algorithms use in their wind speed retrievals and how these channels get weighted in the MLE. CAP includes the scatterometer VV-pol and the radiometer V-pol into their MLE. We do not. We include the scatterometer VV-pol in the roughness correction in addition to the HH wind speed in the form of a correction table, ΔE_{W1}, as discussed in section 6.1. The reason is the poor correlation of σ_{0VV} with wind speed, in particular at cross-wind observations. In addition, the values of our estimated errors for σ_0 and ΔE_{W0} in the MLE are different than those used in the CAP algorithm, which includes only the instrument noise figures. These are the K_p-values for the radar measurements and the noise equivalent delta temperature (NEDT) values for the radiometer measurements after applying appropriate noise reduction to account for the sampling onto the 1.44 s observation cycle. The CAP noise values are about 2–4 times smaller than our estimated error values. Finally, the CAP retrieval process is a one-step process that retrieves wind speed and ocean surface salinity simultaneously by performing a MLE in two-dimensional space that is spanned by both parameters. Our algorithm first retrieves wind speed and then removes the surface roughness effect from the measured TB using this wind speed. The roughness corrected TB is then used in the salinity retrieval.

Examples of how the differences of the GMF and algorithms impact the wind speed performance are shown in Table 1 and Figure 12. In both cases, exactly the same observations were used for the results of our algorithm as for the CAP Version 2.5.1 data. The most noticeable differences between CAP V2.5.1 and our algorithm are:

1. The standard deviations of the Aquarius-WindSat wind speed differences: 0.70 m/s (HHH winds), 0.80 m/s (HH winds), 0.93 m/s (CAP V2.5.1). These differences reflect a higher noise in the CAP retrievals.
2. The unphysical shape of the wind speed distribution, which deviates from the expected Rayleigh shape. This issue has already been noted in the CAP wind speed validation study [*Fore et al*., 2014].

8. Summary and Conclusions

In order to measure sea surface salinity with the required accuracy it is necessary to remove the ocean surface roughness signal from the observed Aquarius brightness temperatures. This requires an accurate knowledge of the signal itself as well as the ocean surface wind speed.

We have derived a GMF for this signal at L-band frequencies. The derivation is based on a match-up data set consisting of one full year of Aquarius radiometer TB and radar backscatter σ_0 measurements with satellite microwave imager (WindSat, F17 SSMIS) wind speeds in rain-free scenes. It also includes important ancillary information from collocated HYCOM salinity, NOAA SST, NCEP GDAS wind speed and direction fields and the NOAA Wave Watch III significant wave height model.

The central step in the roughness correction is the combination of Aquarius HH-pol scatterometer and H-pol radiometer measurements to derive a wind speed, called HHH wind. The accuracy of the roughness correction algorithm can be further improved by incorporating additional information from the scatterometer VV-pol and wave height data. We have demonstrated that a roughness correction that is able to use active in addition to passive L-band measurement reduces the RMS error of the ocean salinity measurement by about 40%. This is an important step toward reaching the strict Aquarius mission requirement of 0.2 psu salinity accuracy and gives the Aquarius instrument a clear advantage over SMOS, which has no scatterometer.

Our study has also indicated that the L-band third Stokes parameter has a sizeable wind direction signal above 10 m/s.

As part of assessing the accuracy of the roughness correction, we have performed a validation of the Aquarius HHH wind speed against WindSat and buoy wind speeds. We have seen that its precision is at least as good as that of many other active and passive microwave satellite wind speeds (WindSat, SSMIS, QuikSCAT, ASCAT). Preliminary results even indicate promising performance in storms with high winds and intense rain, though a systematic study of rain splashing effects on the ocean surface and its effect on wind speed measurements is still outstanding.

The data volume is limited in case of Aquarius due to its very narrow Earth swath. In addition, the resolution (85–125 km) is not particularly good. The Aquarius HHH wind speed is therefore not as useful as a geophysical product as other satellite wind speeds. However, we expect that a similar wind speed accuracy can be achieved in case of the SMAP (Soil Moisture Active Passive) mission [*Entekhabi et al.*, 2010], whose launch is scheduled for fall 2014. SMAP has a 1000 km wide swath and will provide combined active/passive observations at 40 km resolution, which will make the SMAP wind speed a useful product for meteorological and oceanographical applications. The better resolution of SMAP will result in a slightly noisier wind speed than for Aquarius but, considering the excellent precision we have obtained for the Aquarius wind speeds, that is not expected to be a major issue.

Acknowledgments
This work has been supported by NASA contract NNG04HZ29C. We would like to thank the members of the Aquarius cal/val and science teams, in particular Gary Lagerloef, David LeVine, Simon Yueh, Yi Chao, Tong Lee, Shannon Brown, Emmanuel Dinnat, Alex Fore, Hsun-Ying Kao, and Sid Misra for numerous useful discussions.

References

Abe, H., and N. Ebuchi (2013), Evaluation of sea surface salinity observed by Aquarius and SMOS, paper presented at the SMOS-Aquarius Workshop, IFREMER, Brest, France. [Available at http://www.smosaquarius2013.org/.]

Biswas, S., L. Jones, D. Rocca, and J.-C. Gallio (2012), Aquarius/SAC-D microwave radiometer (MWR): Instrument description & brightness temperature calibration, in *The IEEE International Geoscience and Remote Sensing Symposium*, pp. 2956–2959, IEEE, Munich, doi:10.1109/IGARSS.2012.6350705.

Boutin, J., N. Martin, G. Reverdin, X. Yin, and F. Gaillard (2013), Sea surface freshening inferred from SMOS and ARGO salinity: Impact of rain, *Ocean Sci.*, *9*, 183–192, doi:10.5194/os-9-183-2013.

Camps, A., et al. (2004), The WISE 2000 and 2001 field experiments in support of the SMOS mission: Sea surface L-band brightness temperature observations and their application to multi-angular salinity retrieval, *IEEE Trans. Geosci. Remote Sens.*, *42*(4), 804–823, doi:10.1109/TGRS.2003.819444.

Dinnat, E., and D. Le Vine (2007), Effects of the antenna aperture on remote sensing of sea surface salinity at L-band, *IEEE Trans. Geosci. Remote Sens.*, *45*(7), 2051–2060, doi:10.1109/TGRS.2007.890807.

Dinnat, E., J. Boutin, G. Caudal, and J. Etcheto (2003), Issues concerning the sea emissivity modeling at L-band for retrieving surface salinity, *Radio Sci.*, *38*(4), 8060, doi:10.1029/2002RS002637.

Dinnat, E., D. Le Vine, S. Abraham, P. De Matthaeis, and C. Utku (2012), Comparison of Aquarius measurements and radiative transfer models at L-band, in *Proceedings of the 12th Specialist Meeting on Microwave Radiometry and Remote Sensing of the Environment (MicroRad)*, pp. 1–4, IEEE, Rome, doi:10.1109/MicroRad.2012.6185231.

Entekhabi, D., et al. (2010), The soil moisture active passive (SMAP) mission, *Proc. IEEE*, *98*(5), 704–716, doi:10.1109/JPROC.2010.2043918.

Etcheto, J., E. Dinnat, J. Boutin, A. Camps, J. Miller, S. Contardo, J. Wesson, J. Font, and D. Long (2004), Wind speed effect on L-band brightness temperature inferred from EuroSTARRS and WISE 2001 field experiments, *IEEE Trans. Geosci. Remote Sens.*, *42*(10), 2206–2213, doi:10.1109/TGRS.2004.834644.

Font, J., G. Lagerloef, D. Le Vine, A. Camps, and O. Zanife (2004), The determination of surface salinity with the European SMOS space mission, *IEEE Trans. Geosci. Remote Sens.*, *42*(10), 2196–2205, doi:10.1109/TGRS.2004.834649.

Fore, A., S. Yueh, W. Tang, A. Hayashi, and G. Lagerloef (2014), Aquarius wind speed products: Algorithms and validation, *IEEE Trans. Geosci. Remote Sens.*, *52*(5), 2920–2926, doi:10.1109/TGRS.2013.2267616.

Guimbard, S., J. Gourrion, M. Portabella, A. Turiel, C. Gabarro, and J. Font (2012), SMOS semi-empirical ocean forward model adjustment, *IEEE Trans. Geosci. Remote Sens.*, *50*(5), 1676–1687, doi:10.1109/TGRS.2012.2188410.

Hersbach, H., A. Stoffelen, and S. de Haan (2007), An improved C-band scatterometer ocean geophysical model function: CMOD5, *J. Geophys. Res.*, *112*, C03006, doi:10.1029/2006JC003743.

Hilburn, K., and F. Wentz (2008), Intercalibrated passive microwave rain products from the unified microwave ocean retrieval algorithm (UMORA), *J. Appl. Meteorol. Climatol.*, *47*(3), 778–794, doi:10.1175/2007JAMC1635.1.

Hollinger, J. (1971), Passive microwave measurements of sea surface roughness, *IEEE Trans. Geosci. Electron.*, *9*(3), 165–169, doi:10.1109/TGE.1971.271489.

Isoguchi, O., and M. Shimada (2009), An L-band ocean geophysical model function derived from PALSAR, *IEEE Trans. Geosci. Remote Sens.*, *47*(7), 1925–1936, doi:10.1109/TGRS.2008.2010864.

Klobuchar, J. (1987), Ionospheric time delay algorithm for single frequency GPS users, *IEEE Trans. Aerosp. Electron. Syst.*, *23*(3), 325–331, doi:10.1109/TAES.1987.310829.

Lagerloef, G., and H.-Y. Kao (2013), Aquarius data release V2.0: Validation analysis, paper presented at the SMOS-Aquarius Workshop, IFREMER, Brest, France. [Available at http://www.smosaquarius2013.org/.]

Lagerloef, G., et al. (2008), The Aquarius/Sac-D mission: Designed to meet the salinity remote-sensing challenge, *Oceanography*, *21*(1), 68–81, doi:10.5670/oceanog.2008.68.

Le Vine, D., and S. Abraham (2002), The effect of the ionosphere on remote sensing of sea surface salinity from space: Absorption and emission at L Band, *IEEE Trans. Geosci. Remote Sens.*, *40*(4), 771–782, doi:10.1109/TGRS.2002.1006342.

Le Vine, D., E. Dinnat, S. Abraham, P. De Matthaeis, and F. Wentz (2011), The Aquarius simulator and cold-sky calibration, *IEEE Trans. Geosci. Remote Sens.*, *49*(9), 3198–3210, doi:10.1109/TGRS.2011.2161481.

Mannucci, A., B. Wilson, D. Yuan, C. Ho, U. Lindqwister, and T. Runge (1998), A global mapping technique for GPS-derived ionospheric total electron content measurements, *Radio Sci.*, *33*(3), 565–582, doi:10.1029/97RS02707.

Meissner, T. (2014), Performance degradation and Q/C flagging of Aquarius L2 salinity retrievals, *RSS Tech. Rep. 01202014*, Remote Sens. Syst., Santa Rosa, Calif. [Available at ftp://podaac-ftp.jpl.nasa.gov/allData/aquarius/docs/v3/.]

Meissner, T., and F. Wentz (2002), An updated analysis of the ocean surface wind direction signal in passive microwave brightness temperatures, *IEEE Trans. Geosci. Remote Sens.*, *40*(6), 1230–1240, doi:10.1109/TGRS.2002.800231.

Meissner, T., and F. Wentz (2004), The complex dielectric constant of pure and sea water from microwave satellite observations, *IEEE Trans. Geosci. Remote Sens.*, *42*(9), 1836–1849, doi:10.1109/TGRS.2004.831888.

Meissner, T., and F. Wentz (2006), Polarization rotation and the third Stokes parameter: The effects of spacecraft attitude and Faraday rotation, *IEEE Trans. Geosci. Remote Sens.*, *44*(3), 506–515, doi:10.1109/TGRS.2005.858413.

Meissner, T., and F. Wentz (2009), Wind vector retrievals under rain with passive satellite microwave radiometers, *IEEE Trans. Geosci. Remote Sens.*, *47*(9), 3065–3083, doi:10.1109/TGRS.2009.2027012.

Meissner, T., and F. Wentz (2012), The emissivity of the ocean surface between 6 and 90 GHz over a large range of wind speeds and earth incidence angles, *IEEE Trans. Geosci. Remote Sens.*, *50*(8), 3004–3026, doi:10.1109/TGRS.2011.2179662.

Meissner, T., D. Smith, and F. Wentz (2001), A 10-year intercomparison between collocated SSM/I oceanic surface wind speed retrievals and global analyses, *J. Geophys. Res.*, *112*, C11731, doi:10.1029/1999JC000098.

Meissner, T., F. Wentz, and D. Draper (2011a), GMI calibration algorithm and analysis theoretical basis document, Version F, *RSS Rep. 111311*, Remote Sens. Syst., Santa Rosa, Calif. [Available at http://www.remss.com/papers/gmi_ATBD.pdf.]

Meissner, T., L. Ricciardulli, and F. Wentz (2011b), All-weather wind vector measurements from intercalibrated active and passive microwave satellite sensors, in *IEEE International Geoscience and Remote Sensing Symposium*, pp. 1509–1511, IEEE, Vancouver, B. C., Canada, doi:10.1109/IGARSS.2011.6049354.

Meissner, T., F. Wentz, G. Lagerloef, and D. LeVine (2012a), The Aquarius salinity retrieval algorithm, in *Microwave Radiometry and Remote Sensing of the Environment (MicroRad)*, pp. 1–3, IEEE, Rome, doi:10.1109/MicroRad.2012.6185227.

Meissner, T., F. Wentz, K. Hilburn, G. Lagerloef, and D. LeVine (2012b), The Aquarius salinity retrieval algorithm, in *IEEE International Geoscience and Remote Sensing Symposium*, pp. 386–388, IEEE, Munich, doi:10.1109/IGARSS.2012.6351557.

Misra, S., and C. Ruf (2008), Detection of radio-frequency interference for the Aquarius radiometer, *IEEE Trans. Geosci. Remote Sens.*, *46*(10), 3123–3128, doi:10.1109/TGRS.2008.920371.

Monahan, E., and I. O'Muircheartaigh (1980), Optimal power-law description of oceanic whitecap coverage dependence on wind speed, *J. Phys. Oceanogr.*, *10*, 2094–2099, doi:10.1175/1520-0485(1980)010<2094:OPLDOO>2.0.CO;2.

Moore, R., I. Birrer, E. Bracalente, G. Dome, and F. Wentz (1982), Evaluation of atmospheric attenuation from SMMR brightness temperature for the SEASAT satellite scatterometer, *J. Geophys. Res.*, *87*(C5), 3337–3354, doi:10.1029/JC087iC05p03337.

Piepmeier, J., D. Long, and E. Njoku (2008), Stokes antenna temperatures, *IEEE Trans. Geosci. Remote Sens.*, *46*(2), 516–527, doi:10.1109/TGRS.2007.909597.

Piepmeier, J., S. Brown, J. Gales, L. Hong, G. Lagerloef, D. Le Vine, P. de Matthaeis, T. Meissner, R. Bindlish, and T. Jackson (2013), Aquarius radiometer post-launch calibration for product version 2, *Aquarius Proj. Doc. AQ-014-PS-0015*. [Available at http://podaac.jpl.nasa.gov/SeaSurfaceSalinity/Aquarius.]

Powell, M., S. Houston, L. Amat, and N. Morisseau-Leroy (1998), The HRD real-time hurricane wind analysis system, *J. Wind Eng. Ind. Aerodyn.*, *77/78*, 53–64, doi:10.1016/S0167–6105(98)00131-7.

Reul, N., J. Tenerelli, B. Chapron, D. Vandemark, Y. Quilfen, and Y. Kerr (2012), SMOS satellite L-band radiometer: A new capability for ocean surface remote sensing in hurricanes, *J. Geophys. Res.*, *117*, C02006, doi:10.1029/2011JC007474.

Reynolds, R., and T. Smith (1994), Improved global sea surface temperature analyses using optimum interpolation, *J. Clim.*, *7*(6), 929–948, doi:10.1175/1520-0442(1994)007<0929:IGSSTA>2.0.CO;2.

Ricciardulli, L., and F. Wentz (2011), Reprocessed QuikSCAT (V04) wind vectors with Ku-2011 Geophysical Model Function, *RSS Tech. Rep. 043011*, Remote Sens. Syst., Santa Rosa, Calif. [Available at http://www.remss.com/papers/rsstech/2011_043011_ricciardulli_qscat_ku2011.pdf.]

Rybicki, G., and A. Lightman (1979), *Radiative Processes in Astrophysics*, John Wiley & Sons, N. Y.

Verspeek, J., A. Stoffelen, M. Portabella, H. Bonekamp, C. Anderson, and J. F. Saldana (2010), Validation and calibration of ASCAT using CMOD5.n, *IEEE Trans. Geosci. Remote Sens.*, *48*(1), 386–395, doi:10.1109/TGRS.2009.2027896.

Weissman, D., B. Stiles, S. Hristova-Veleva, D. Long, D. Smith, K. Hilburn, and W. Jones (2012), Challenges to satellite sensors of ocean winds: Addressing precipitation effects, *J. Atmos. Oceanic Technol.*, *29*(3), 356–374, doi:10.1175/JTECH-D-11–00054.1.

Wentz, F. (1991), A simplified wind vector algorithm for satellite scatterometers, *J. Atmos. Oceanic Technol.*, *8*(5), 697–704, doi:10.1175/1520-0426(1991)008<0697:ASWVAF>2.0.CO;2.

Wentz, F. (2005), The effects of cloud and rain on the Aquarius salinity retrieval: Algorithm theoretical basis document, *RSS Tech. Rep. 3031805*, Remote Sens. Syst., Santa Rosa, Calif. [Available at http://www.remss.com/papers/aquarius/rain_effect_on_salinity.pdf.]

Wentz, F., and D. Smith (1999), A model function for the ocean-normalized radar cross section at 14 GHz derived from NSCAT observations, *J. Geophys. Res.*, *105*(C5), 11,499–11,514, doi:10.1029/98JC02148.

Wentz, F., et al. (2012), Aquarius salinity retrieval algorithm: Algorithm theoretical basis document, Version 2, Addendum I (2012), Addendum II (2013), Addendum III (2014), *RSS Tech. Rep. 082912*, Remote Sens. Syst., Santa Rosa, Calif. [Available at http://podaac.jpl.nasa.gov/SeaSurfaceSalinity/Aquarius.]

Yin, X., J. Boutin, N. Martin, and P. Spurgeon (2012), Optimization of L-band sea surface emissivity models deduced from SMOS data, *IEEE Trans. Geosci. Remote Sens.*, *50*(5), 1414–1426, doi:10.1109/TGRS.2012.2184547.

Yueh, S. (2000), Estimates of Faraday rotation with passive microwave polarimetry for microwave remote sensing of Earth surfaces, *IEEE Trans. Geosci. Remote Sens.*, *38*(5), 2434–2438, doi:10.1109/36.868900.

Yueh, S., and J. Chaubell (2012), Sea surface salinity and wind retrieval using combined passive and active L-band microwave observations, *IEEE Trans. Geosci. Remote Sens.*, *50*(4), 1022–1032, doi:10.1109/TGRS.2011.2165075.

Yueh, S., S. Dinardo, A. Fore, and F. Li (2010), Passive and active L-band microwave observations and modeling of ocean surface winds, *IEEE Trans. Geosci. Remote Sens.*, *48*(8), 3087–3100, doi:10.1109/36.752213.

Yueh, S., A. Fore, A. Freedman, J. Chaubell, W. Tang, and G. Neumann (2012), *Aquarius Scatterometer Algorithm: Theoretical Basis Document, Version 1*, Jet Propul. Lab. [Available at http://podaac.jpl.nasa.gov/SeaSurfaceSalinity/Aquarius.]

Yueh, S., W. Tang, A. Fore, G. Neumann, A. Hayashi, A. Freedman, J. Chaubell, and G. Lagerloef (2013), L-band passive and active microwave geophysical model functions of ocean surface winds and applications to Aquarius retrieval, *IEEE Trans. Geosci. Remote Sens.*, *51*(9), 4619–4662, doi:10.1109/TGRS.2013.2266915.